

**STUDY OF NORMALIZATION TECHNIQUES USING LOW AND  
HIGH ENERGY X-RAY FLUORESCENCE EXCITATION BEAMS  
WITH STANDARD SAMPLES**

**BY**

**BRYN RANKIN**

A thesis submitted to the  
Department of Physics  
Mount Allison University  
in partial fulfillment of the requirements for the  
Bachelor of Science degree with Honours  
April 13, 2023

## ABSTRACT

X-Ray fluorescence is gaining popularity in the scientific community as it is portable, non-invasive, and inexpensive to operate. Rigorous method analysis is needed to accurately assess health and mineral conditions in people or crops through concentrations of various elements. The current study examines the role of the 6.4keV X-ray fluorescence (XRF) excitation beam in the analysis of low atomic number ( $Z$ ) elements and its comparison to the 17.48keV excitation beam for these elements. Fifty okra samples were analyzed using XRF and results were compared to inductively coupled plasma mass spectrometry (ICP-MS) values through linear correlation plots. The correlations for calcium, potassium, and phosphorus, revealed that the 6.4keV excitation beam, was better suited for elements up to but not including chromium. The low energy beam had an average  $R^2$  value of 0.74 whereas the high energy beam had an  $R^2$  of 0.52 for the okra samples. The same procedure was used to examine standard caprine horn samples where only calcium was examined. These supported the use of the low energy beam for low  $Z$  elements with an average  $R^2$  value of 0.45 compared to the high energy  $R^2$  value of 0.26. Normalization of the data was required and four methods, Region of Interest (ROI), Molybdenum or Iron, Scatter Peak, and total area ratio (TAR) were created and tested to determine which produced normalized counts with the best correlation to ICP-MS. Linear correlations of the okra samples indicated the ROI method was most promising for studying low  $Z$  elements while using the low energy X-ray fluorescence excitation beam. The goat horn samples indicated the Fe method provided the best correlations though all  $R^2$  were similar and the relative uncertainties were twice the okra. More research is needed to determine the potential of the ROI normalization method with higher atomic number elements.

## ACKNOWLEDGMENTS

There are numerous people I would like to thank for their dedication and assistance to my success in this project. First and foremost, this endeavor would not have been possible without Dr. David Fleming. I am sincerely grateful for his invaluable patience and guidance. Additionally, I would like to thank the Natural Sciences and Engineering Research Council for providing the funding of this investigation along with the Okra in a Refugee Context in East Africa and the Development and Characterization of Keratinized Reference Materials studies for supplying the samples. The University of Jaen was instrumental in this project as they produced the ICP-MS results for the okra. I had the pleasure of working with many talented individuals in the physics department over the last few years, to whom I am appreciative for their time and assistance. A special thanks goes to my lab mates; I will forever remember the time we wasted playing trivia in the medical physics lab. I am especially grateful for my family, both at home and those I found in Sackville, for their support.

# Contents

<b>ABSTRACT</b>	<b>i</b>
<b>ACKNOWLEDGMENTS</b>	<b>ii</b>
<b>TABLE OF CONTENTS</b>	<b>iii</b>
<b>LIST OF FIGURES</b>	<b>vi</b>
<b>LIST OF TABLES</b>	<b>viii</b>
<b>GLOSSARY</b>	<b>ix</b>
<b>1 INTRODUCTION</b>	<b>1</b>
1.1 Calcium . . . . .	1
1.1.1 Role in human body and sources . . . . .	1
1.1.2 Effects of deficiency or toxicity . . . . .	4
1.2 Phosphorus . . . . .	6
1.2.1 Role in human body and sources . . . . .	6
1.2.2 Effects of deficiency or toxicity . . . . .	8
1.3 Potassium . . . . .	9
1.3.1 Role in human body and sources . . . . .	9
1.3.2 Effects of deficiency or toxicity . . . . .	11
1.4 Standard samples . . . . .	12
1.4.1 Okra . . . . .	12
1.4.2 Caprine Horn . . . . .	13
1.5 Main objective of study . . . . .	13
<b>2 THEORY</b>	<b>15</b>
2.1 X-Rays . . . . .	15
2.1.1 Bremsstrahlung radiation . . . . .	15
2.1.2 Characteristic X-Rays . . . . .	16
2.1.3 Characteristic X-Ray nomenclature . . . . .	17
2.2 X-ray interactions . . . . .	17

2.2.1	Rayleigh scattering . . . . .	17
2.2.2	Compton scattering . . . . .	18
2.2.3	Photoelectric absorption . . . . .	18
2.2.4	Fluorescent yield and Auger electrons . . . . .	19
2.3	Portable X-Ray Fluorescence . . . . .	19
2.3.1	High energy beam . . . . .	21
2.3.2	Low energy beam . . . . .	21
2.4	Absorption edges . . . . .	22
<b>3</b>	<b>METHODS</b>	<b>24</b>
3.1	Samples . . . . .	24
3.1.1	Collection and preparation of samples . . . . .	24
3.1.2	Extra okra samples . . . . .	25
3.2	Measurements with XRF . . . . .	26
3.3	PyMca fittings . . . . .	27
3.3.1	Long vs short tail . . . . .	28
3.4	Normalization methods . . . . .	28
3.4.1	ROI . . . . .	28
3.4.2	Mo or Fe . . . . .	32
3.4.3	Scatter peaks . . . . .	33
3.4.4	Total counts . . . . .	34
3.5	ICP-MS measurements . . . . .	35
3.6	Uncertainty in normalized counts and ICP-MS . . . . .	35
3.6.1	Uncertainty in ROI and TAR . . . . .	36
3.6.2	Uncertainty in Fe/Mo and Scatter Peak . . . . .	37
3.7	Data comparison . . . . .	37
<b>4</b>	<b>RESULTS</b>	<b>39</b>
4.1	Okra . . . . .	39
4.1.1	Calcium linear correlations . . . . .	41
4.1.2	Phosphorus linear correlations . . . . .	42
4.1.3	Potassium linear correlations . . . . .	44
4.2	Caprine horn . . . . .	47
4.2.1	Low energy beam & high energy beam linear correlations . . . . .	51

<b>5</b>	<b>DISCUSSION</b>	<b>55</b>
5.1	Low energy beam vs high energy beam . . . . .	55
5.1.1	Okra samples . . . . .	55
5.1.2	Caprine horn samples . . . . .	57
5.2	Normalization method comparison . . . . .	58
5.2.1	Okra samples using low energy beam . . . . .	58
5.2.2	Okra samples using high energy beam . . . . .	59
5.2.3	Caprine horn samples using low energy beam . . . . .	60
5.2.4	Caprine horn samples using high energy beam . . . . .	62
<b>6</b>	<b>CONCLUSION</b>	<b>64</b>
	<b>REFERENCES</b>	<b>66</b>

## List of Figures

2.1	The X-ray fluorescence process with the ejection of an inner-shell electron and the replacement by an outer-shell electron with the release of a characteristic X-ray [Weindorf and Chakraborty, 2020]. . . . .	16
2.2	HD Mobile X-ray fluorescence system with okra sample on the measuring platform. . . . .	21
2.3	Absorption edge of iodine demonstrated through the relationship between absorption and X-ray energy. Vertical lines indicate mean energy levels of polychromatic 80 kilovoltage peak (kVp) and 120 kVp spectra while using dual energy computed tomography [Elbanna et al., 2020].	23
3.1	Left side of PyMca program showing checked boxes. . . . .	29
3.2	Configure section of the Advanced fit and the many possible fitting options. . . . .	30
3.3	ROI bounds on either side of the coherent scatter peak on the X-ray spectrum and table showing the corresponding energies of the bounds and net counts of the peak. . . . .	31
3.4	Mo or Fe method of normalization. Calibration of spectrum showing the chosen peak for normalization. . . . .	33
4.1	Spectrum of the energy (keV) and un-normalized counts for okra sample 50 using the 6.4 keV X-ray beam. . . . .	40
4.2	Spectrum of the energy (keV) and un-normalized counts for okra sample 50 using the 17.48 keV X-ray beam. . . . .	40
4.3	Normalization method comparison using the relationship between normalized counts and ICP-MS concentration of Ca in okra with the 6.4 keV X-ray beam. . . . .	41
4.4	Normalization method comparison using the relationship between normalized counts and ICP-MS concentration of Ca in okra with the 17.48 keV X-ray beam. . . . .	42
4.5	Normalization method comparison using the relationship between normalized counts and ICP-MS concentration of P in okra with the 6.4 keV X-ray beam. . . . .	43

4.6	Normalization method comparison using the relationship between normalized counts and ICP-MS concentration of P in okra with the 17.48 keV X-ray beam. . . . .	44
4.7	Normalization method comparison using the relationship between normalized counts and ICP-MS concentration of K in okra with the 6.4 keV X-ray beam. . . . .	45
4.8	Normalization method comparison using the relationship between normalized counts and ICP-MS concentration of K in okra with the 17.48 keV X-ray beam. . . . .	45
4.9	Spectrum of the un-normalized counts and energy (keV) for goat horn sample 1 using the 6.4 keV X-ray beam. . . . .	49
4.10	Spectrum of the un-normalized counts and energy (keV) for goat horn sample 1 using the 17.48 keV X-ray beam. . . . .	50
4.11	Normalization method comparison using the relationship between normalized counts and ICP-MS concentration of Ca in goat horn with the 6.4 keV X-ray beam. . . . .	52
4.12	Normalization method comparison using the relationship between normalized counts and ICP-MS concentration of Ca in goat horn with the 17.48 keV X-ray beam. . . . .	52

## List of Tables

2.1	Summary of K-edge values for the three elements of interest Ca, P, and K. . . . .	23
3.1	PyMca detector tab specifications. . . . .	27
3.2	PyMca details for scatter peak normalization. . . . .	34
4.1	Summary of $R^2$ values for linear correlations of okra between normalized counts and ICP-MS results for each element and normalization method using the 6.4 keV X-ray beam. . . . .	46
4.2	Summary of $R^2$ values for linear correlations of okra between normalized counts and ICP-MS results for each element and normalization method using the 17.48 keV X-ray beam. . . . .	47
4.3	Summary of relative uncertainties in normalized counts for okra using the 6.4 keV and 17.48 keV X-ray beam. . . . .	47
4.4	Summary of $R^2$ values for linear correlations of goat horn between normalized counts and ICP-MS results for Ca using each normalization method. . . . .	53
4.5	Summary of relative uncertainties in normalized counts for goat horn using the 6.4 keV and 17.48 keV X-ray beam. . . . .	53

## GLOSSARY

AAS	Atomic Absorption Spectrometry
ADP	Adenosine Diphosphate
ATP	Adenosine Triphosphate
Ca	Calcium
CVD	Cardiovascular Disease
DCC	Doubly Curved Crystal
DNA	Deoxyribonucleic Acid
ICP-MS	Inductively Coupled Plasma Mass Spectrometry
ICP-OES	Inductively Coupled Plasma Optical Emission Spectrometry
INAA	Instrumental Neutron Activation Analysis
K	Potassium
LVH	Left Ventricular Hypertrophy
NYSDOH	New York State Department of Health
P	Phosphorus
PXRF	Portable X-Ray Fluorescence
RM	Reference Materials
ROI	Region Of Interest
TAR	Total Area Ratio
XOS	X-Ray Optical Systems
XRF	X-Ray Fluorescence
Z	Atomic Number

# Chapter 1

## INTRODUCTION

The following study is focused on calcium, phosphorus, and potassium, through measurements of their concentration in different reference materials by X-ray fluorescence (XRF) using two different X-ray beam energies.

### 1.1 Calcium

Calcium has many important uses in the human body including nerve conduction, muscle contraction, and structural support in the skeletal system. It has been determined that calcium may have a key role in reducing the risk of certain chronic diseases. Major sources of calcium available to humans are in dairy foods or in supplements. The deficiency or surplus of calcium otherwise known as hypocalcemia and hypercalcemia respectively can be detrimental to one's physical health.

#### 1.1.1 Role in human body and sources

Calcium is well known for promoting bone growth but it also has many other health benefits that are often unknown by the general public. The many processes that calcium is engaged in comprise structural support, mitosis, muscle contraction, nerve conduction, and blood coagulation [Miller et al., 2001].

The amount of calcium suggested by health professionals varies for different age groups. Children ages 1-3 years need 500 mg, 800 mg for 4-8 years old, 1300 mg for 9-18, 1000 mg for 19-50, and finally 1200 mg for people over 51 years old per day. For all age groups it has been found that men ingest more calcium than women which is

likely a result of their higher energy requirements or that women are more efficient in terms of energy conservation. The teenage years are crucial for high calcium consumption when children undergo puberty and rapid skeletal growth. Ingesting the suggested calcium amounts during this time will help prevent future skeletal issues such as osteoporosis [Miller et al., 2001]. With 1 kg of calcium in the human body, over 99 percent of it resides in the bone and teeth. It increases the strength of the bones by increasing its mass in the form of hydroxyapatite. The quantity of calcium ingested during childhood and adolescence impacts how the skeleton retains calcium and peak bone mass in early adult years. In the 4 years encompassing the greatest skeletal growth, teens gain 39 percent of their total body bone minerals. This suggests that insufficient intake of calcium during this time could lead to decreased peak bone mass as well as increased risk of osteoporotic fractures [Weaver et al., 2016]. The bioavailability of calcium depends on intestinal absorption and the excretion of calcium in urine. To help calcium absorption it has been commonly suggested that vitamin D be taken in combination with calcium [Theobald, 2005].

Calcium is a signalling molecule in many processes in the body including mitosis. During mitosis DNA replicates and separates as the parent cell divides into two daughter cells. This is an important event in the body for growth and replacing damaged cells. A signal is created when calcium floods the intracellular matrix through regulation channels of the plasma membrane as well as the intracellular matrix of the endoplasmic reticulum. Calcium plays a role in cell division through the phosphoinositide-calcium-calmodulin signalling pathway. This path is involved in the beginning of mitosis and the onset of anaphase [Whitaker and Larman, 2001].

Another important role of calcium in the body is in muscle contraction. During contraction of muscle, stimulation causes calcium from inside the sarcoplasmic reticulum in striated muscles or vesicles in smooth muscle to be released into the sarcoplasm.

Calcium removes the inhibitory regulatory proteins troponin and tropomyosin to create a cross link between actin and myosin. Once the muscle contraction is complete, calcium is then removed from the area and travels back to its original location [Szent-Györgyi, 1975].

When one is cut and a blood vessel is injured, it starts to bleed and clotting factors are necessary to stop the bleeding. Molecules are released from the damaged tissue and activate the clotting factors and platelets that are flowing through the bloodstream. Calcium is one of these molecules that are required for activation. It binds to phospholipids to provide the building blocks for other coagulation factors. Calcium is also needed in the complex that converts prothrombin to thrombin which creates a fibrin network to stabilize clots [Palta et al., 2014].

As established, calcium is an important nutrient in the human body. The best way to receive calcium in the diet is through the consumption of dairy products. Dairy products and in particular milk, are often considered controversial in terms of human consumption. It is commonly said that cow's milk was not meant to be drank by humans, humans are the only animals that continue drinking milk after infancy, or milk creates a greater risk of fractures. What one must consider however is that most of what people consume today is not what it was many years ago and humans are the only ones who have learned agriculture and the domestication of dairy cows. Finally, many experiments have been done to investigate the role cow's milk has in the increased risk of fractures but there is no overall consensus and a fair number of experiments have bias. Cow's milk should continue to be part of the human diet particularly for children and populations with increased risk of osteoporotic fractures [Fardellone et al., 2017].

Calcium rich foods include milk, milk products, soft bone fish, dark leafy green vegetables, tofu, as well as calcium fortified foods. Though many vegetables contain

calcium some also have phylates and oxalates that can reduce the absorption of calcium in the intestines. Many vegetables do not allow for the same quantity of calcium to be absorbed that milk does. The greater the amount of oxalic acid in a food the less calcium can be absorbed from it. Vitamin D is often added to milk as it aides in the absorption and regulation of calcium. Calcium supplements can also be taken to prevent deficiency.

Recently there has been a rise in calcium-fortified food which introduces new problems such as calcium toxicity, lower calcium absorption, and the decrease in consumption of other important nutrients. These come in the form of calcium carbonate, citrate, citrate malate, phosphate, gluconate, lactate, or calcium magnesium carbonate. The supplements are not intended to act as a substitute for naturally calcium rich foods but an addition to the diet [Miller et al., 2001].

### **1.1.2 Effects of deficiency or toxicity**

Low calcium levels and intake do not cause many symptoms unless left untreated in the long term. Lack of calcium can increase the risk of osteoporosis, and hypertension while increased calcium levels can lead to strokes and kidney stones [Miller et al., 2001].

Osteoporosis is when bone thins and is at risk for fracture. The disease is most common for older adults and most often affects the spine and hips. Many times there are no symptoms of osteoporosis until a minor bump or fall leads to a fracture which in turn can cause other issues such as chronic pain. Osteoporosis occurs when the hard shell of bone called the cortical bone becomes thinner and the spongy inside, the trabecular bone, is broken down faster than it can be made [National Institute on Aging, n.d., Sunyecz, 2008].

When one's blood pressure is elevated continually this is called hypertension and

increases the potential for cardiovascular or kidney diseases [Cormick et al., 2015]. High blood pressure is typically a result of an unhealthy diet or not enough physical activity. Similar to osteoporosis, there are no symptoms of hypertension and it is only noticed through monitoring the blood pressure. Having a high blood pressure can lead to a reduction in the elasticity of arteries which in turn causes less blood and oxygen to reach important organs [CDC, 2021]. It has been found on numerous occasions that both humans and animals with higher calcium levels are less likely to have hypertension [Kim et al., 2012; McCarron et al., 1982]. As well, an increase in calcium intake along with a low fat diet will reduce blood pressure in a short period of time and prevent the onset of hypertension [Cormick et al., 2015; Miller et al., 2001].

Strokes are one of the most common causes of death in the world and are due to a lack of oxygenated blood flowing to the brain [Guo et al., 2015; Johnson et al., 2016]. There are two ways in which a stroke can occur, both within the brain. The first is an ischemic stroke where a blood clot or plaque prevents blood from flowing in arteries. The second is a hemorrhagic stroke when a blood vessel ruptures often from high blood pressure. Depriving the brain of oxygen can cause cells to die and damage normal brain functions. There exist transient ischemic attacks or mini-strokes that can act as a warning for future strokes [CDC, 2022]. In all cases the symptom onset is very rapid and can consist of different neurological signs such as the numbness of the face or limbs, difficulty walking or speaking, or blurred vision [Markus, 2008]. Though the role calcium plays in a stroke is still controversial it has been determined that calcium supplements can increase the risk of occurrence [Pu et al., 2016; Reid et al., 2011].

## 1.2 Phosphorus

Phosphorous is abundant in the human body and involved in many pathways. It is necessary for normal cell function, has roles in the skeletal system, and is a key nutrient for energy production [Bird and Eskin, 2021; Takeda et al., 2004]. Phosphorous can be found in protein-rich foods as well as an additive in processed food. Blood tests that show high phosphorous levels are correlated with cardiovascular disease, kidney disease, and the harm of bone metabolism [Uribarri and Calvo, 2014; Vorland et al., 2017]. Hypophosphatemia is a lack of phosphorous in the blood and can result in proximal myopathy, a weakness in upper and/or lower limbs. It is also associated with rhabdomyolysis [Amanzadeh and Reilly, 2006; Takeda et al., 2012].

### 1.2.1 Role in human body and sources

Phosphorous is crucial for humans but due to high consumption of processed food many people have it in excess in their body. Phosphorous is used regularly in energy production, blood buffering, and many structural aspects [Kendrick et al., 2011].

In a cell phosphate has many purposes. It is capable of turning adenosine diphosphate (ADP) into adenosine triphosphate (ATP) which provides energy for many processes through oxidative phosphorylation. During oxidative phosphorylation electrons are moved through a pathway, releasing energy and creating an electrochemical gradient. The build up of energy allows for the final phosphate to be added to ADP [Bose et al., 2003; Calvo and Lamberg-Allardt, 2015; Qadeer and Bashir, 2022]. Phosphate is one of three major components of deoxyribonucleic acid (DNA) along with a sugar and a nitrogen base. DNA holds the blueprints for all structures and functions in a living organism. Since phosphate is a building block for DNA it is also important for cell replication and growth as well as playing a role in regulating gene transcription [Bird and Eskin, 2021; Calvo and Lamberg-Allardt, 2015].

Phosphorus is often recognized as part of the phospholipid bilayer that makes up the cell membrane and is important for cell functions but it is also vital for skeletal structures. In bone, phosphorus is present as hydroxyapatite, a form of calcium-phosphate [Michigami et al., 2018]. During bone mineralization, osteoblasts release matrix vesicles which then, through a series of activations, can absorb calcium and phosphate ions. The calcium and phosphate combine to create hydroxyapatite that can then be deposited on the surface of bone. This action mineralizes the bone [Mahamid et al., 2011; Michigami and Ozono, 2019].

The recommended daily allowance of phosphorous ranges from about 500 mg for children 4-8, 1250 mg for ages 9-18, and 700 mg for those over 19 years of age [Calvo and Lamberg-Allardt, 2015]. Phosphate additives make up a large amount of the daily phosphorous intake, estimated between 10%-50% [Office of Dietary Supplements, 2021]. The recent average for phosphorous intake in adults is about 1400 mg, twice the recommended value. There exists a balance of phosphorous in the body with absorption from the diet, urine excretion, and its movement between tissues and cells in the body. The kidneys are the main regulators of these processes. Keeping the balance of phosphorus with calcium is important to reduce harmful hormones circulating in the body [Uribarri and Calvo, 2014].

As mentioned, phosphorus is widely used as an additive in food for preservation, colour enhancement, or to stabilize frozen food. The inorganic phosphate is commonly found in highly processed foods. As for natural phosphorus, it can be found in many dairy and meat products as well as fish, eggs, and vegetables. Dairy products form 20% of the total phosphorus intake whereas vegetables contribute only 5% because phosphorus is present as phytate and less digestible [Uribarri and Calvo, 2014]. Natural phosphorus absorbs more slowly and less efficiently than the additives. This indicates that a vegetarian diet may have less phosphorus and decrease the risk of

health conditions [Calvo and Uribarri, 2013].

### **1.2.2 Effects of deficiency or toxicity**

Hypophosphatemia is often caused by rare diseases or a combination of decreased dietary intake and another issue. It can also be from difficulties absorbing phosphorous in the intestines, a movement of phosphorous into cells, or an increase of phosphorous in the urine. If left untreated hypophosphatemia can lead to rhabdomyolysis where damaged muscle tissue release their contents including protein and electrolytes. These then can travel through the blood stream injuring the heart or kidneys. When muscle cells are hurt the cell membrane is penetrated, decreasing ATP inside the cells and allowing an influx of calcium ions and giving rise to cell lysis. Rhabdomyolysis occurs as a result of the lack of phosphorous and in turn muscle ATP [Amanzadeh and Reilly, 2006; Cabral et al., 2020; Takeda et al., 2012].

Phosphorous additives are intended to increase the shelf life of many foods as well as to make some creamier or add flavour and colour. Instead these additions can make phosphorous levels rise in the body which may lead to negative effects on bones or osteoporosis. A high phosphorous, low calcium diet along with hyperparathyroidism was found to reduce bone mass in mice [Vorland et al., 2017]. Phosphorous added to foods is more rapidly absorbed completely compared to natural phosphorous. High bodily phosphorous is associated with disrupting calcium balance and thus reduces the calcium in bone [Calvo and Tucker, 2013].

Cardiovascular disease (CVD) is an illness that affects the heart or blood vessels. High levels of phosphorous in the blood have been connected to left ventricular hypertrophy (LVH) where the wall of the main chamber in the heart thickens resulting in poor circulation and high pressure in the heart. LVH increases the risk of cardiovascular events [Kendrick et al., 2011]. There are two methods in which phosphorous may

cause CVD, vascular calcification and modulation of circulating hormones. Phosphorus creates changes in the vascular smooth muscle cells by influencing what genes are transcribed. The vascular smooth muscle cells release proteins that inhibit calcification in the vasculature. This calcification can result in narrowing arteries and veins. The second method is through the inactivation of vitamin D. Low vitamin D levels have been associated with CVD [Gutiérrez, 2013; Judd and Tangpricha, 2009; Kendrick et al., 2011].

## **1.3 Potassium**

Potassium is a common ion in the human body involved in maintaining cell membrane potentials, muscle and nerve excitation, as well as the intracellular osmolarity. Potassium is commonly found in various fruits and vegetables as well as different meats. It has roles in blood pressure and the cardiovascular system, antioxidant properties, and controlling blood glucose levels [Ekmekcioglu et al., 2016].

### **1.3.1 Role in human body and sources**

Potassium was once a more common nutrient in the human diet but with increased consumption of processed foods levels have drastically decreased as it is removed from these types of food. It is an important staple in the diet with roles in controlling cell membrane potentials and the fluid levels in cells.

Cells maintain ion potentials through a balance of sodium-potassium adenosine triphosphatase pumps bringing potassium into the cells and excreting sodium. Potassium can also flow out through potassium channels when necessary. The water content, hormones, insulin levels, and ion concentrations play important roles in the balance [Ekmekcioglu et al., 2016]. During the sodium-potassium exchange, an electrical potential is created which can give rise to the conduction of nerve impulses.

The potential controls voltage-gated calcium ion channels which leads to muscle contraction. Potassium can then leave the cell, reducing the electric potential gradient. This exchange is key for many processes including muscle contractions, heartbeats, and neural signaling [Jackson, 2017, Kowey, 2002].

Potassium also has a vital role in maintaining osmotic pressure, ensuring the proper water content in cells and body compartments. Potassium is the major ion of the interacellular fluid [Pohl et al., 2013]. Osmosis occurs when there is high ion concentration on one side of the cell membrane and water flows through the membrane towards the ions to reduce the concentration. When the body is full of water the blood is diluted and the sodium concentration is low compared to intracellular concentrations. Water can then enter the cells to reduce the concentration gradient on either side of the cell membrane. Sodium is the main ion in osmosis but it is controlled through its relationship with potassium.

The dietary recommendation of potassium is 3.8 g per day for ages 4-8 years old, 4.5 g for ages 9-13, and over 14 years of age the recommended value is 4.7 g per day. The greatest contributions of potassium to the diet are potatoes, drinks such as tea, coffee and fruit juice, as well as meats. Many processed foods contain potassium as a preservative in the form of potassium chloride. A diet with more potassium chloride has increased sodium intake and decreased potassium intake [Lanham-New et al., 2012]. Examination of kidney functions shows that they conserve sodium and excrete potassium which may indicate that the human diet was once plant-based with high potassium and low sodium levels [Ekmekcioglu et al., 2016]. Potassium primarily resides intracellularly in the muscle and bone while it can be excreted in the urine, feces, and sweat [Lanham-New et al., 2012]. Many studies suggest that the best way to increase the intake of potassium is through the consumption of fruits and vegetables as they contain potassium in the form of potassium citrate [Ekmekcioglu

et al., 2016; He and MacGregor, 2008; Lanham-New et al., 2012].

### 1.3.2 Effects of deficiency or toxicity

A deficiency of potassium can be a result of the excess processed foods in the diet though due to its availability in many foods, it is uncommon. Studies have shown that a diet focused on fruits and vegetables with low fat results in lower blood pressure [Ekmekcioglu et al., 2016]. As stated earlier, these foods are high in potassium leading to the conclusion that increasing potassium intake can lower blood pressure and thus decrease risk of CVD [Ekmekcioglu et al., 2016]. The effectiveness of lowering the risk of CVD is greatly increased when a potassium-rich diet is combined with decreased sodium intakes. Strokes are also less frequently observed in those with a lower blood pressure as a result of higher potassium [Aburto et al., 2013; Lanham-New et al., 2012].

It has been found that those with lower potassium may also have glucose intolerance where blood sugar levels are elevated. This is through mechanisms impairing insulin secretion. Upon supplementation with potassium these effects are lessened and may prevent the onset of diabetes [He and MacGregor, 2008]. In the pancreas,  $\beta$  cells create insulin that control blood sugar levels. When there are normal levels of potassium there is an increase of extracellular potassium on the  $\beta$  cell membrane causing depolarization, triggering the cell to produce insulin. With a lack of potassium this mechanism is impeded [Ekmekcioglu et al., 2016].

Toxicity is often associated with potassium supplements in addition to a regular potassium-rich diet. Due to the efficient excretion processes of the kidneys, it is highly uncommon to have toxic amounts of potassium in the blood. Excess potassium in the body is called hyperkalaemia and is most often due to dysfunction of kidneys or medication side effects and can be difficult to diagnose [He and MacGregor, 2008].

Hyperkalemia can cause irregular heartbeats, muscle weakness, and paralysis [Parham et al., 2006]. Treatments for hyperkalemia include administering calcium to stabilize cell membranes, insulin to move extracellular potassium inside cells, and diuretics to remove the potassium from the body [Kim et al., 2023].

## 1.4 Standard samples

Standard samples are reference materials that contain known concentrations of different elements.

### 1.4.1 Okra

As part of the mallow family along with cacao and cotton, okra is a vegetable with edible seed pods. Many South Sudanese refugees bring okra seeds with them to cultivate them in their new settlements. Okra is capable of growing in regions with intermittent rainfall and poor soils. Many settlements grow okra along with pumpkin, and beans in gardens for personal use. Okra is one of the crops in the African orphan crops consortium that aims to improve the diversity and nutrition of food crops. Okra is a calcium rich food which aides in the common calcium deficiency in many people. It is full of minerals, vitamins, antioxidants, and fiber. Okra is often sun-dried for sauce, soup, or just sliced. Not only is it an important staple, okra is also a source of income for those who grow it. The purpose of the original study of the okra samples used here was to investigate the mineral composition of okra and its contribution to the overall absorption of different elements in the body [Woldetsadik et al., 2021]. As a result of this study, a variety of elements and their concentrations were characterized accurately in the okra samples using a method known as inductively coupled plasma mass spectrometry (ICP-MS).

Okra is commonly used as a pain reliever in Eastern countries. This is likely due

to its antimicrobial and anti-inflammatory properties. Okra has also been found to be a source of antioxidants along with phenolic compounds and flavonoid derivatives which are thought to lower the risk of cancer. Okra is a good source of vitamin K [Habtamu Fekadu Gemedede et al., 2014]. Vitamin K is an important contributor to bone formation and blood clotting. It can help strengthen bones and may help prevent breaks and osteoporosis.

#### **1.4.2 Caprine Horn**

Unlike the okra study, the goat horn investigation was aimed from its original conception to create reference materials (RM) for trace element analysis. The goat horn samples were collected from 11 goats, some dosed orally with lead, that were tended to by the the New York State Department of Health (NYS DOH) Wadsworth Center. The purpose of these goats was to produce lead enriched reference blood for the NYS DOH blood lead proficiency testing program. All animal protocols and ethical considerations were followed for the care and use of the goats [Tehrani et al., 2020]. The goat horn powder was created to be Keratin Matrix RMs to compare analysis methods of trace elements in nail or hair. These samples were in use to investigate if XRF was capable of examining zinc levels in human nail and hair samples. The XRF was determined to be useful and with concentration conversions, capable of providing accurate zinc concentrations in keratin based samples [Fleming et al., 2023]. For the purpose of this thesis, elemental concentrations determined using the method of ICP-MS will be used from the caprine horn powder samples.

### **1.5 Main objective of study**

The purpose of the study was primarily to investigate the role of the low energy XRF beam in the analysis of samples and how its results compared to the results from the

high energy beam. This required examining low atomic number ( $Z$ ) elements which have scarcely been done previously with the XRF. Much of the previous research focus has been on higher  $Z$  elements such as zinc, arsenic, selenium, and lead [Fleming et al., 2023]. This study provided the opportunity to see the roles of the low  $Z$  elements in body and if the concentrations in hair or nail could be used to provide information on human conditions. As well, the study allowed investigation of different energies of excitation as noted above.

As the study progressed it also encompassed determining what normalization technique provided the optimal results. Past research with the higher energy excitation beam included a normalization method using the total area under the whole energy spectrum created from the XRF characteristic X-rays and scattered radiation [Fleming et al., 2023]. In this study, extra normalization methods were created to investigate which was optimal for the low and high energy beams. The results of the study could lead to new ways of collecting and analyzing the XRF data and provide a novel method of examining concentrations of low atomic number elements in patients.

## Chapter 2

### THEORY

#### 2.1 X-Rays

Wilhelm Roentgen, a physics professor at the University of Würzburg, discovered X-rays in 1895. He noticed a screen fluorescing during an experiment to create cathode rays in a Crookes tube. He called these X-rays, referring to the unknown radiation. X-rays gave the ability to produce images of bones under flesh. This allowed for viewing foreign bodies which was revolutionary in the medical society [Arne Hessenbruch, 2002]. X-rays have wavelengths between 0.01-10 nm and energy from 100 eV-100 keV. The electromagnetic spectrum region that makes up X-rays is split between higher and lower energies where soft X-rays are 100-1000 eV and hard x-rays have energy between 5-10 keV [Smith, 2000]. X-rays can be generated through two methods relevant to the XRF system used in the study: the emission of a characteristic X-ray and Bremsstrahlung radiation.

##### 2.1.1 Bremsstrahlung radiation

Bremsstrahlung radiation is also known as braking radiation due to the deceleration of electrons as they are deflected from their original path by an electric field of atoms. When the electron slows down, it releases energy as a continuous radiation spectrum [Stacy and Vestrand, 2003]. In the XRF system, electrons collide with the anode inelastically and decelerate releasing Bremsstrahlung radiation. The electrons may interact with more than one nucleus, any of which can release X-rays with various energies depending on the atom size and proximity.

### 2.1.2 Characteristic X-Rays

The second method of X-ray generation is through the ionization of atoms in the anode in the X-ray tube. The electron beam travels to the anode and collides with an inner-shell electron in an atom. The electron is ejected from the atom and a higher energy electron from an outer-shell falls to replace it. As a result of this, the replacement electron loses energy in the form of an X-ray with energy equal to the difference between the outer-shell and inner-shell binding energy. This process can be seen in Figure 2.1 and can also occur in a sample, with the difference being that in a sample, the excitation is caused by an X-ray beam, not an electron beam.

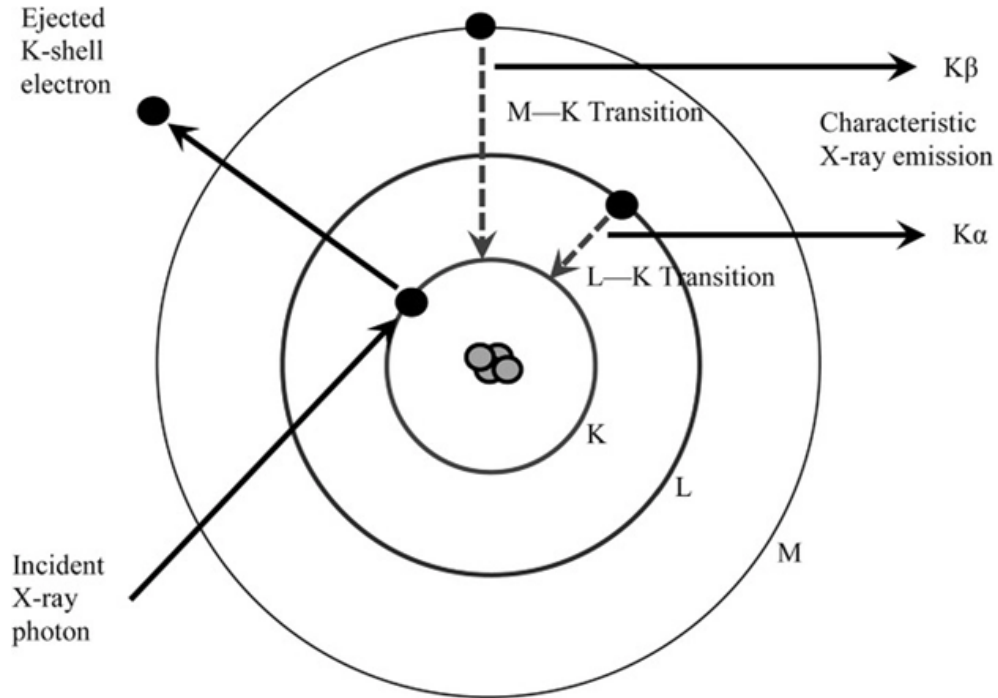


Figure 2.1: The X-ray fluorescence process with the ejection of an inner-shell electron and the replacement by an outer-shell electron with the release of a characteristic X-ray [Weindorf and Chakraborty, 2020].

Most electron shell energy differences result in electromagnetic radiation in the X-ray region though it is possible that a photon in the visible region can be released. Electron shells are always at the same energy levels for the same elements due to the

quantization of atomic orbitals, and thus the X-rays released will be characteristic for a certain element. This differs from the continuous Bremsstrahlung radiation as it is discrete. The anode of the XRF system under consideration in this thesis is composed of molybdenum. Depending on the mode of operation, an iron target may also be placed within the X-ray beam path. Either molybdenum or iron characteristic X-rays are then used, creating a monoenergetic beam capable of exciting a sample.

### **2.1.3 Characteristic X-Ray nomenclature**

There are many characteristic X-rays from each element due to the variety of shell combinations possible. The energy of the characteristic X-ray is unique for each electron transition in each element. To organize the X-rays, the Siegbahn notation is used in this study. The first part of the system labels the final shell of the transitioning electron as K, L, M, N, O corresponding to shells  $n= 1, 2, 3, 4, 5$  respectively. A Greek letter is used as a subscript to indicate the origin of the transitioning electron. One shell higher than the final shell is  $\alpha$ , two shells is  $\beta$ , and three shells is  $\gamma$ . For example, a  $K_\alpha$  X-ray is released from an electron drop from the L shell to the K shell.

## **2.2 X-ray interactions**

Once an X-ray beam is created, we need to consider how the X-rays interact within a sample. When an X-ray beam strikes a sample it can pass through, scatter, or be absorbed. All of these can occur in the XRF system.

### **2.2.1 Rayleigh scattering**

The first type of scattering of the X-ray beam occurs in an elastic collision between the X-rays and electrons in the sample. The interaction is between the photon and tightly bound electrons which are rigid during the collision. Rayleigh scattering has the

requirement that the particle the radiation is scattered by has a much smaller radius than the wavelength of the radiation for it to occur [Eremin, 2005; J. E. Fernández, 1995]. Due to the elastic collision no energy is lost and the Raleigh radiation has the same energy as the incident X-rays [Margui and Van Grieken, 2013].

### **2.2.2 Compton scattering**

Similar to Rayleigh scattering, Compton scatter occurs between X-rays and electrons. The difference between the two is the Compton collision is inelastic and so photon energy is lost during the interaction. This implies the Compton peak in an XRF spectrum will appear at a lower energy than the Rayleigh peak. During the collision the X-ray transfers some of its energy to an outer-shell electron allowing it to escape while the photon is scattered [Margui and Van Grieken, 2013; Dutton, 2010].

### **2.2.3 Photoelectric absorption**

The photoelectric effect forms the foundations of XRF. During photoelectric absorption, an X-ray is incident on an atom and is completely absorbed during the collision. The photon imposes all its energy on an electron allowing it to overcome binding energy and escape the atom. This removal ionizes the atom making it unstable and can only occur when the photon has more energy than the binding energy of the electron. The photoelectron will have kinetic energy equal to the difference between the photon and the electron binding energy [Stacy and Vestrand, 2003]. The energy is in the electronvolt range and thus only photons from the X-ray or ultraviolet range of the electromagnetic spectrum can create photoelectrons [Margaritondo, 2005]. The ionized atom can become stable again through two processes: the release of characteristic X-rays as described earlier, or the Auger effect. In both cases an electron from an outer shell falls to replace the ejected one.

#### 2.2.4 Fluorescent yield and Auger electrons

Photoelectric absorption results in an electron from an outer-shell filling an empty spot in an inner-shell. The energy that is sometimes released in the form of an X-ray can instead be transferred to an outer electron. This is an Auger electron and is ejected during the process, similar to the original photoelectric process. The Auger effect competes with XRF as the excess energy is used to remove the Auger electron. Due to the competing processes, the intensity of the characteristic X-rays are dependent on how successful each process is in an atom. Fluorescent yield is the probability that a characteristic X-ray is emitted from a given element. This number changes depending on the element and is almost 1 for high Z elements, but about 0.01 for some low Z elements. The small fluorescent yield for low Z elements decreases the sensitivity of the XRF system for these elements [Margui and Van Grieken, 2013].

### 2.3 Portable X-Ray Fluorescence

As a fairly new approach to elemental analysis, portable XRF (PXRF) is non-invasive compared to other methods of biomarker analysis such as a blood test. There is potential for XRF in the use of zinc in hair or nail samples as a biomarker to determine the concentration in the patient and analyse if they have abnormal results. XRF has many advantages despite lacking the same precision and accuracy as the “gold standards”: inductively coupled plasma mass spectrometry (ICP-MS), inductively coupled plasma optical emission spectrometry (ICP-OES), atomic absorption spectrometry (AAS), and instrumental neutron activation analysis (INAA). The PXRF has the capability of taking measurements in the field and providing fast results while being simple to operate. The XRF is also fairly inexpensive compared to the more established techniques and can work with small sample sizes [Fleming et al., 2023].

In this study, the HD Mobile X-ray fluorescence system (X-ray Optical Systems; East Greenbush, NY, USA) was used to measure the concentrations of calcium, phosphorus, and potassium in okra and goat horn powder. The system is monoenergetic such that instead of using a continuous energy spectrum resulting from Bremsstrahlung radiation, only characteristic X-rays are used to excite the samples. The anode of the X-ray tube consists of molybdenum which has a characteristic X-ray energy of 17.48 keV. When the lower 6.4 keV beam is desired for use an iron target is placed in front of the molybdenum anode.

The XRF system uses Doubly Curved Crystal (DCC) optics to provide a narrow high intensity beam. Bragg's law forms the basis for these crystals where they can reflect intense radiation at specific wavelengths and angles. The DCCs are toroidally curved to focus the monochromatic beam in three dimensions creating an ideal beam with a diameter of approximately 1mm capable of taking measurements of small samples such as hair or nail. DCCs increase sensitivity of measurements through the elimination of background X-ray scattering [Chen et al., 2008; X-ray Optical Systems, 2008].

As stated, the XRF system has the capability operating in handheld mode, for taking measurements in the field (for example, soil analysis). The XRF is regularly in tabletop mode for measurements, and that is the mode used in this study as seen in Figure 2.2. As a result of being portable, the PXRF has a smaller X-ray tube and the detector is contained within the device itself. The XRF used in this study has a 25  $mm^2$  silicon drift detector [Fleming et al., 2023]. The silicon drift detector consists of an electron depleted piece of silicon in an electric field perpendicular to the silicon surface. The electric field pushes electrons released from the absorption of ionizing radiation towards the anode, generating current of varying amounts corresponding to the energy of the characteristic X-ray detected. The system then takes the counts

and exports them as an Excel sheet that can be used in an analyzing software called PyMca.



Figure 2.2: HD Mobile X-ray fluorescence system with okra sample on the measuring platform.

### 2.3.1 High energy beam

Past sample analyses have been done exclusively with the high energy beam of the XRF system. The high energy beam corresponds to the  $K_{\alpha}$  x-ray of molybdenum with energy of 17.48 keV. This is the result of a molybdenum anode in the X-ray tube. This energy is often high enough to excite all the elements of interest including zinc, arsenic, selenium, and lead.

### 2.3.2 Low energy beam

In the current study, the low energy beam was explored for the first time in the medical physics lab. The low energy beam corresponds to the  $K_{\alpha}$  of iron, having an

energy of 6.4 keV. An iron target is placed in front of the molybdenum anode. Some of the original X-ray beam passes through the target and optics as well, resulting in a small component of the beam which has the energy of the higher beam. This is evident through visual analysis of the spectra showing small scattering peaks at 17.48 keV. The low energy beam limits what elements can be examined as it does not have enough energy to excite elements above chromium. However, for low  $Z$  elements, the low energy beam will be more efficient at exciting characteristic X-rays.

## 2.4 Absorption edges

Absorption edges arise from the photoelectric effect and are where the absorption of X-rays is greatly increased at a specific energy [Yamashita et al., 1998]. The absorption edge is unique to each element and is at the energy required to sufficiently excite inner-shell electrons such that they can escape the atom or transition to an upper shell. This energy is otherwise known as the binding energy of the electron. The inner-shell of an atom is called the K-shell therefore this effect can also be described as the K-edge [Kvick, 1999].

As mentioned, the binding energy of the K-shell is unique for each element and it increases as the atomic number increases. For a given element, there is a sharp increase in absorption of X-rays as their energy reaches the K-edge then the absorption decreases as the energy is increased past this value. This can be seen in Figure 2.3 where the K-edge of iodine occurs just after 30 keV.

The most efficient removal of an electron occurs when exactly the binding energy is transferred to the electron. The probability of removal is highest at this point then decreases as the energy gets higher. This then leads to the conclusion that the X-ray beam with energy closer to K-edge energy of the elements of interest would be more efficient at creating characteristic X-rays from a given sample. The K-edge values of

Ca, P, and K can be seen in Table 2.1.

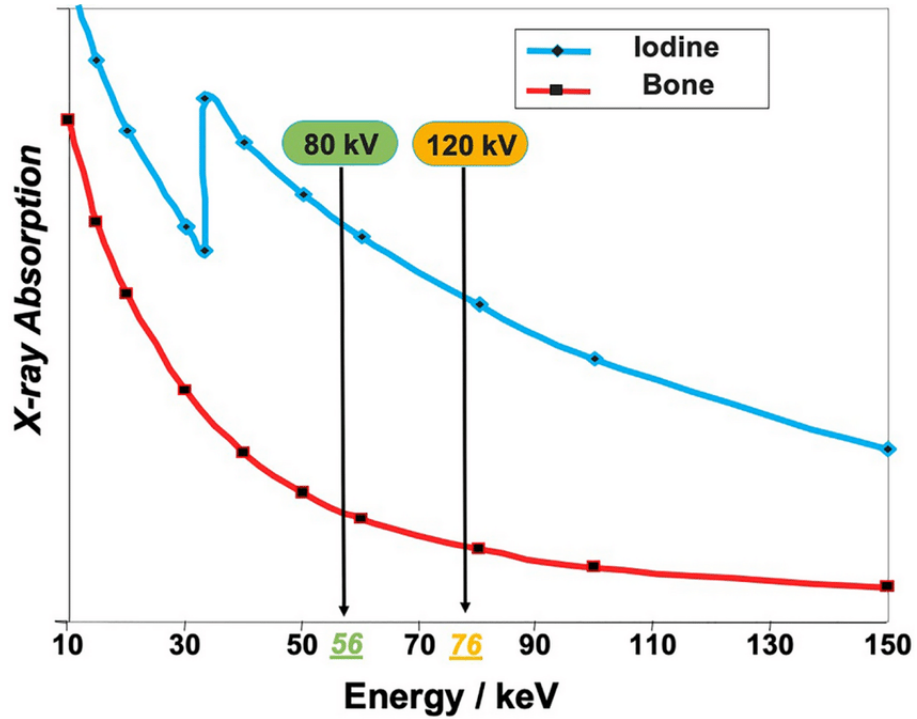


Figure 2.3: Absorption edge of iodine demonstrated through the relationship between absorption and X-ray energy. Vertical lines indicate mean energy levels of polychromatic 80 kilovoltage peak (kVp) and 120 kVp spectra while using dual energy computed tomography [Elbanna et al., 2020].

Element	K-edge (keV)
Ca	4.038
P	2.146
K	3.608

Table 2.1: Summary of K-edge values for the three elements of interest Ca, P, and K.

## Chapter 3

### METHODS

#### 3.1 Samples

The study, Okra (*Abelmoschus esculentus*) in a refugee context in East Africa: Kitchen gardening helps with mineral provision [Woldetsadik et al., 2021], provided 50 okra samples sourced from 4 refugee settlements. Two of the four samples came from Kule and Tierkidi in Ethiopia and the other two from Rhino and Imvepi in Uganda. Thirteen caprine horns were collected post-mortem from 11 goats cared for by the NYS DOH Wadsworth Center [Tehrani et al., 2020]. The horns were combined to give four standard reference materials.

##### 3.1.1 Collection and preparation of samples

In total, 48 okra pod samples were collected from the 4 refugee settlements in East Africa. Pods were collected through two methods due to the lack of standing okra trees during the season. The first group of pods were taken directly off the trees and placed into pools of 4-5 pods per sample. The second group of pods were sourced from refugees' sun-dried stores and the equivalent of 4-5 fresh pods were pooled again. A total of 12 sample cups were collected from Kule and Tierkidi each while 13 and 11 were collected from Rhino and Imvepi respectively. The samples were oven dried and ground. The okra was then distributed to X-ray fluorescence sample cells (SCP Science, Canada), and covered with a 4  $\mu\text{m}$ -thick prolene film. Each sample cup was labeled with the first being designated 01.

The horns were removed from 11 goat skulls by the New York State Department

of Health using a Stryker autopsy saw post-mortem and wiped using “Ghost Wipe” lead dust wipes to remove contaminants from the outer surface. A Dremel tool fitted with a diamond disk blade was used to slice the horns longitudinally before removing the bony core of the goat horn. The remaining horn was then cut into rectangular sections with the same tool. These were then placed in  $H_2O_2$  for an hour to remove exogenous contamination, blood, and remaining epidermis. The horn sections were then rinsed with double de-ionized water and air dried.

The dried goat horns were frozen with liquid nitrogen or overnight in a freezer at  $-80^\circ\text{C}$ . The horns were placed in the Retsch SM 2000 Cutting Mill for grinding. They were re-frozen and milled in the same tool with a 2.0 mm grate. The samples were further milled with the Retsch ZM200 Ultra-Centrifugal Mill with Ti sieves and a 0.25 mm grate. Finally the horn powder was oven-dried at  $55^\circ\text{C}$  overnight.

Small portions of the 13 horns were used to determine the lead content for each sample with ICP-MS. The horns were then grouped into four sets to maximize the lead concentration range. The four sets were then sieved to get a fine powder where the larger clumps were crushed with an agate mortar. The samples were placed into 4-mL HDPE vials for storage.

### **3.1.2 Extra okra samples**

As stated before, 48 okra pod samples were collected in total from different regions of Africa and labeled 01 to 048. There were a total of 50 samples received by the medical physics lab at Mount Allison University that were created from the 48 okra pod samples. Two of the samples were sub divided to make duplicates but which two is unknown.

### 3.2 Measurements with XRF

The okra sample cups were measured individually using the HD Mobile X-ray fluorescence system (X-ray Optical Systems; East Greenbush, NY, USA) by placing them on the platform above the X-ray beam window. Each were measured once using the molybdenum target with an energy of 17.48 keV for 180 seconds and again with the iron target with an energy of 6.4 keV for 180 seconds. The substrate was set to plastic to be consistent with previous methods of analysis. Prior to placing the samples on the platform they were tapped, and flipped to remove clumps created during storage. They were positioned on the beam window such that the beam would avoid cracks or inhomogeneity. Ten samples were measured in a row starting at 01 with breaks of 30-60 minutes between sets to prevent overheating.

The goat horn vials were measured starting at NYS RM 18-01 then moving sequentially through the four samples. They were measured once for 180 seconds using the low energy, 6.4 keV beam. They were stored upright while not in use. During the second set of trials they were measured in the same order but three times consecutively instead of once. For the third set of trials, the goat horn powder was again measured in the same order but five times consecutively. This method was repeated with the higher energy, 17.48 keV beam.

An unexpected complication occurred when there was two sheets in the results Excel file for the low energy beam. The first corresponded to the beam warming up and replacing the Mo target with the Fe target for a duration of 10 seconds, while the second was the actual 3 mins measurement with the low energy beam. As this was the initial use of the 6.4 keV beam we were not aware of the second sheet and thus initially used the first sheet data in the analysis. Once this error was found the correct data was used and the analysis was repeated.

### 3.3 PyMca fittings

PyMca takes the counts provided by the XRF and creates a spectral graph depicting the counts with their corresponding energy. The software creates a fitted curve to the data for analysis. The fitted curve provides areas and uncertainties in areas for various energy peaks.

In PyMca the calibration was skipped as batch fitting was performed. Under the Advanced Fit window and in Configuration the Strip Background Width was set to 20 while the Stripping, Escape peaks, Long tail, and Scattering peaks boxes were all checked. Since the iron excitation beam has an energy of 6.4 keV anything above chromium cannot be chosen in the configuration settings. This limits the elements that can be analyzed. The channel range chosen was 100-300 covering elements from silicon to vanadium. Chromium was excluded as the peak was absent from the data spectrum. The  $K_\alpha$  and  $K_\beta$  were selected for each element as it provided a closer fit to the data than the K option. The K option assumes a default ratio between  $K_\alpha$  and  $K_\beta$  detections. In the Detector tab the Spectrometer zero, and Spectrometer gain were set depending on the energy of the beam used for the measurement as seen in Table 3.1 and were fixed. Ignore calibration from input data box was also checked.

Energy (keV)	Spectrometer zero (keV)	Spectrometer gain (keV/ch)
Low 6.4	-0.0540759	0.0176218
High 17.48	-0.0589739	0.017633

Table 3.1: PyMca detector tab specifications.

In the Matrix tab the Incoming Angle was set to 90 degrees, while the Outgoing Angle was 45 degrees. These configurations were saved and used in the batch fittings. The same configurations were used for both okra and goat horn.

### **3.3.1 Long vs short tail**

There has been a long debated dilemma over choosing the long or short tail in the configuration settings. The difference between them is that the area under the short tail is included in the peak counts while the long tail is not. Each measurement was checked for which option was better. The majority of the trials had a better fit with the long tail. Future data may require examination of this to see which should be used for various types of samples [Sharma et al., 2022].

## **3.4 Normalization methods**

Normalization of the counts provided by the XRF is required to reflect a concentration and reduce variability. For example, without normalization small differences in sample thickness might affect results. All methods divide the elemental counts by the value obtained via the normalization method. Different approaches to normalization were explored, and each of these is described below. The ROI, Mo or Fe, and Scatter peaks are all methods to determine the area of the coherent scatter peak for use in normalization where the Total Area Ratio sums the area of all peaks across the energy spectrum for a given measurement. Multiple methods of determining the coherent peak counts were created as the coherent normalization has been promising as seen through consistent results of nail measurements and lower variation due to the clipping thickness [Sharma et al., 2022]. Coherent normalization may be the preferred method compared to other normalization approaches for XRF.

### **3.4.1 ROI**

After collecting the data from the XRF system, it was opened as normal in PyMca. Auto REPLACE was clicked instead of Auto ADD or else it would not give different

values for each trail. The boxes can be seen in Figure 3.1. The axis of the graph

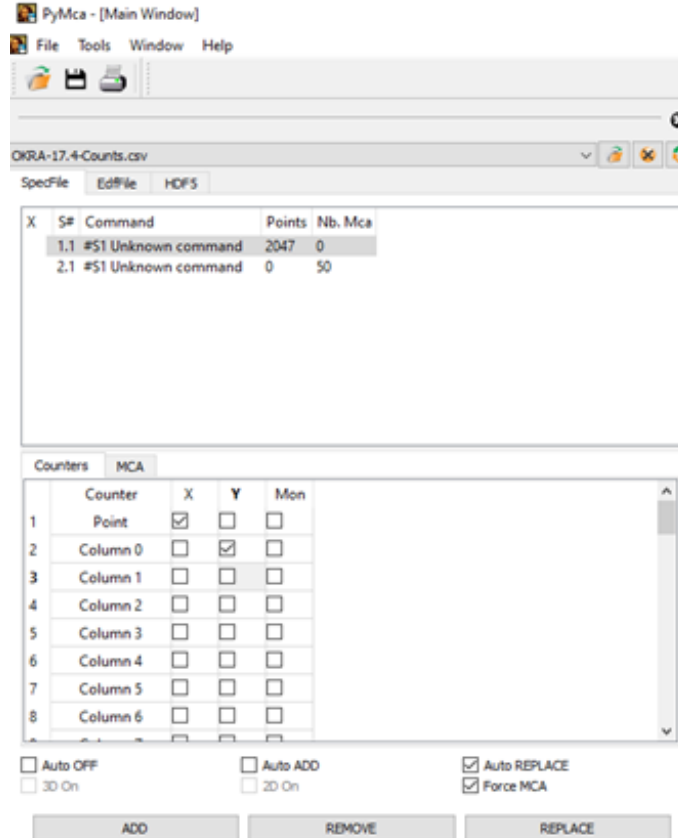


Figure 3.1: Left side of PyMca program showing checked boxes.

on the main page was changed from channel to energy which required a calibration. Calibration could be performed through the calibration drop down and the selection of the Mo, Zn, and Fe peaks with the corresponding transition energy or through the advanced fit button above the graph. In this study, the latter was chosen but it should not create a large discrepancy either way. The advanced fit was clicked without directly calibrating and go into Configure. The configuration file that was previously saved was loaded but a new file could also be created. On the first tab, Fit, the Strip Background Width was 20, the “Limit fitting region to” was not clicked but Stripping, Escape peaks, Long tail, and Scattering peaks were as seen in Figure 3.2.

Under Detector, the correct values for the Spectrometer zero and the Spectrometer

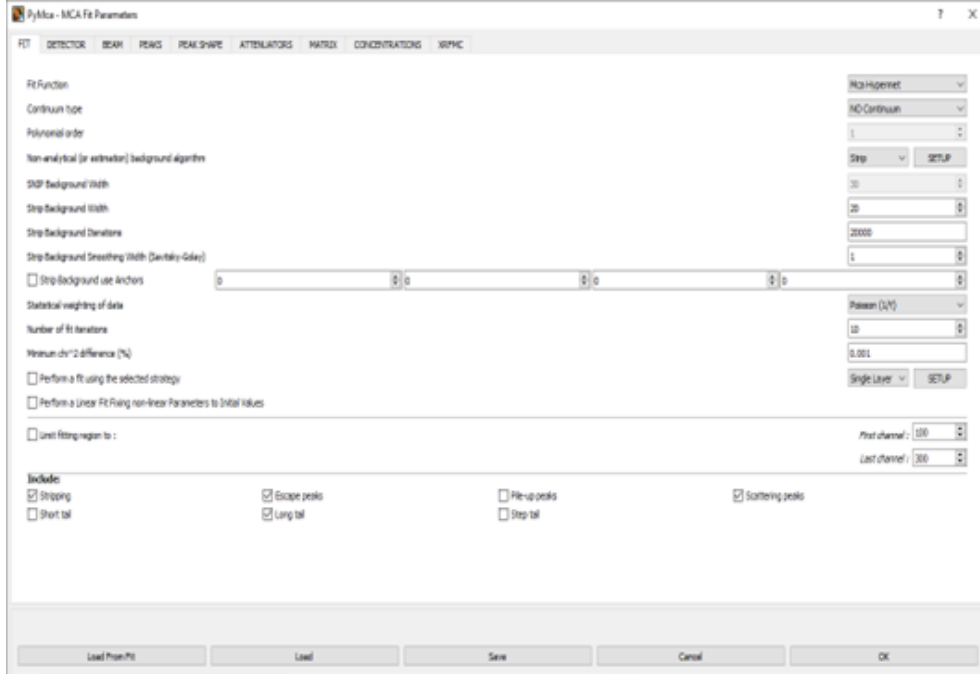


Figure 3.2: Configure section of the Advanced fit and the many possible fitting options.

gain were input depending on the excitation beam. Each were chosen as fixed and the ignore calibration from input data was also clicked on. Under the Matrix tab the incoming angle was 90 degrees, and the outgoing angle was set as 45 degrees. This configuration was saved for other uses. Ok and Fit Again were clicked once all the desired settings were chosen. This calibrated the data.

The x-axis of the graph in the main window no longer had channel and changed to energy. This allows for easy identification of elemental peaks. The bottom right of the window had a section for ROIs of the data and at the bottom of this area was an option to Add ROI. When it was clicked a new row was added to the box under the first ROI which included the entire range. Two blue lines also appeared on the graph with labels ROI min and ROI max. That was how the region of interest is specified. The lines were moved to either side of the coherent peak (Mo for high energy, Fe for low energy). creating a box on the graph zoomed in to get greater accuracy of the

counts for the peak. There was also a possibility to type in the From and To boxes in the new ROI row. The ROI section is depicted in Figure 3.3. The goal of this normalization approach is to use the coherent peak as the normalization.

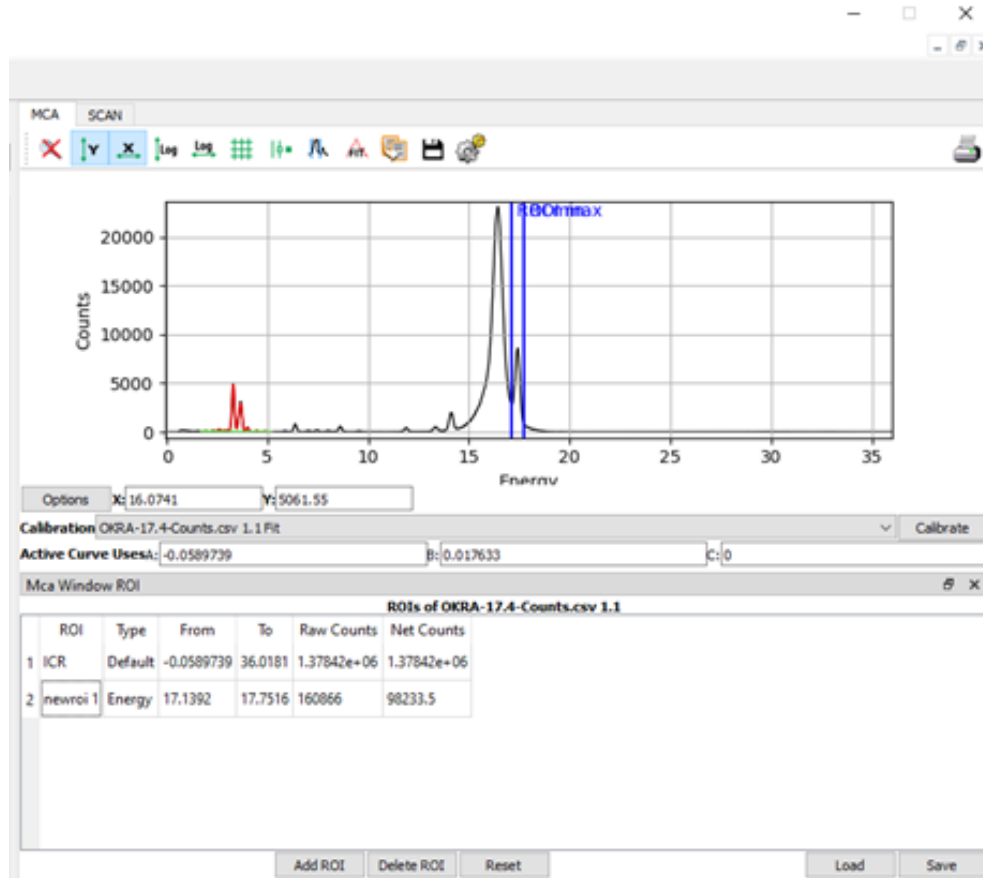


Figure 3.3: ROI bounds on either side of the coherent scatter peak on the X-ray spectrum and table showing the corresponding energies of the bounds and net counts of the peak.

It is possible other elements or the Compton peak may contribute to the counts on the lower end of the peak. For example, in the low energy trials, bounds of 6.05 keV to 6.8411 keV were picked. This removed some counts from the Compton peak and Cr. For the high energy trials, a range of 17.1392 keV to 17.7516 keV was chosen. Zooming in on the fit of the coherent peak back in the Fit window allowed to see where it began and ended.

The count value in the Net Count box was recorded once the desired range was selected. The Net count gives the area under the the curve and above a line that connects the intersections of the bounds and curve. Finally, the next measurement on the left-hand side of the screen was analyzed by clicking the next Y Column and unclicking the current data set. This procedure must be repeated for each measurement.

The uncertainty of the net count was found by taking the square root of the value. The data was analyzed through a batch fitting. The element counts were examined to ensure they had not been reversed during batch fitting. A reversal of data is where the measurement trials appear in the Excel file in the reverse order such that the last trial is recorded first. To normalize, the fit area of the element peaks from each measurement was divided by the net count of the coherent peak corresponding to that measurement.

### **3.4.2 Mo or Fe**

The second method used in the analysis was normalization through a regular fitting of the Fe or Mo peaks which were actually the coherent peaks. To do this, the data was uploaded and the Auto ADD with Force MCA were kept on. The MCA tab on the right-hand section of the screen was checked to ensure the data was there. The method of choosing peaks and matching to the element for calibration was not needed since a batch fit was be performed.

Go directly into the advance fit window where the Strip Background Width should be 20, the range should be the same as mentioned in the previous section. Stripping, Escape peaks, Long tail, and Scattering peaks chosen should be chosen. The detector values are listed in Table 3.1. The beam energy depends on which beam you used. If the low energy beam was used, then instead of 6.4 keV it should be set to 17.48 keV.

If the medium energy beam was used, then instead of 17.48 keV it should be set to 20 keV to get past the  $K_{\beta}$  of Mo. Then under Peaks choose the  $K_{\alpha}$  and  $K_{\beta}$  of Fe or Mo as seen in Figure 3.4.

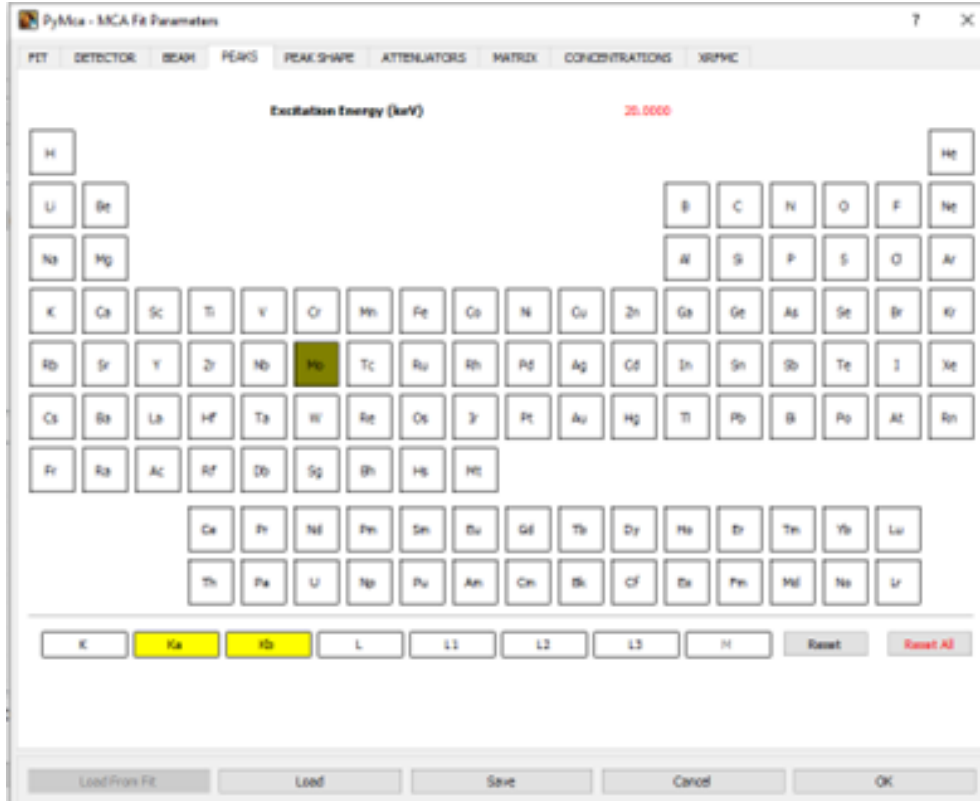


Figure 3.4: Mo or Fe method of normalization. Calibration of spectrum showing the chosen peak for normalization.

Under the Matrix tab the Incoming Angle is 90 degrees, and the Outgoing Angle is 45 degrees. Click OK and Fit Again! to see how it fits the data. The configuration can then be saved and used in batch fittings to get the counts of the coherent peak for each measurement.

### 3.4.3 Scatter peaks

Scatter peaks was the final method that determined the counts of the coherent peak. Once, the data file was upload, the Auto ADD and Force MCA were clicked and

the MCA tab was opened. Again, in this method a batch fit was performed so a calibration was unnecessary. In advance fit the only difference from a normal fit was that the range was moved to focus on the scattering peaks and an element outside the range was chosen.

Inside the configuration window the Strip Background Width was 20, Stripping, Escape peaks, and Scattering peaks were all clicked on. The detector values was the same as mentioned previously. Table 3.2 outlines the changes for this method used in the current study but the range, element, and tail could all be changed to fit individual data better.

	Range (channels)	Beam Energy (keV)	Element Peak	Tail
Low energy	325-385	6.4	Cr	Short
Medium energy	825-1100	17.48	Zn	Long

Table 3.2: PyMca details for scatter peak normalization.

The angles in the Matrix tab were chosen to be the same as before: incoming was 90 degrees, outgoing was 45 degrees. Examination of individual measurements were done to see if Short tail or Long tail was better for the majority. In the main page, Auto REPLACE was picked instead of Auto ADD to accomplish this. Once all the changes were made it was saved to use in a batch fitting.

#### 3.4.4 Total counts

This method used the total area of all the peaks in the energy spectrum. In the file with the counts for each measurement that the XRF system provided, there was a row of slow counts corresponding to the total counts. The elemental counts from PyMca was divided by the slow counts matching each trial. This method is the most simple for implementation, and has often been used in previous studies.

### 3.5 ICP-MS measurements

From each okra sample a small part was removed and digested with 3 mL  $HNO_3$  using a single-reaction chamber system (UltraWave™, Milestone). The samples were then heated to different temperatures for certain amounts of time. They were heated to 100°C for 5 min, 150°C for 7 mins, 180°C for 8 min, 220°C for 5 mins, and finally 220°C for 15 mins. The aliquots were cooled and moved to ICP-MS vials with ultra-pure water. An Agilent 7900 ICP-MS (Agilent Technologies, CA, USA) equipped with a Peltier-cooled quartz spray chamber (Scott type), a quartz torch (2.5 mm i.d.), and a low flow concentric nebulizer (0.2 mL/min) were used to determine the element concentrations at the University of Jaen in Spain.

Goat horn powder was digested before applying the ICP-MS method of analysis. Samples of 200 mg from each horn was added to 35-mL Pyrex digestion vessels with the SP-D (CEM Corporation, Matthews, NC), an automated microwave digestion system. This was placed in a class 4 biohood with 4 mL  $HNO_3$  for 6-12 hrs. In the final hour, 1 mL of 30% (v/v)  $H_2O_2$  for ultra trace analysis (Sigma-Aldrich, Darmstadt, Germany) was incorporated into the mix to fully digest the samples. Once pre-digestion was complete the solutions were digested with the CEM SP-D using a two-stage microwave program. The temperature was increased to 100°C for 4-5 mins, then up to 200°C over 4-5 mins and remained constant for 4-6 mins. DDI water was added to dilute the samples. Finally the solutions were analyzed with ICP-MS.

### 3.6 Uncertainty in normalized counts and ICP-MS

Uncertainties in data can show which methods are more reliable and accurate than others. Uncertainties for the normalized counts from each method and element were

determined and compared to investigate which technique was the most precise. The elemental counts provided by PyMCA had errors given with each element in the batch fit file that was produced. Once the uncertainties in the normalization values were obtained, the uncertainties in the normalized counts were found through the following equation:

$$\delta y = |y| \sqrt{\left(\frac{\delta c}{c}\right)^2 + \left(\frac{\delta n}{n}\right)^2}$$

Here,  $y$  is the normalized count for a given XRF measurement,  $c$  is the elemental count, and  $n$  is the value obtained from the normalization method of choice. Deltas followed by a variable indicate the uncertainty in that variable. The relative uncertainty in the normalized count was found using:

$$\frac{\delta y}{|y|} \cdot 100\%$$

Relative uncertainties were compiled and averaged for each normalization technique and beam energy as well as element. The uncertainties in the ICP-MS measurements were given and so only the relative uncertainties had to be calculated.

### 3.6.1 Uncertainty in ROI and TAR

The net counts from the ROI method and the slow counts from the TAR normalization method did not have errors directly associated with them. For the ROI method, the net count between the specified bounds was shown in PyMCA without an uncertainty value connected to it. There was some error that cannot be quantified due to the personal choice of the upper and lower bounds of the region of interest. The bounds chosen in this study were created based on multiple okra measurements and

examination of the divide between the Compton and coherent scatter peaks. Difficulties come in when one must decide how much the Compton peak is contributing to the counts of the coherent. The choice of bounds may vary depending on the sample type or XRF system used as a result of this. For the TAR normalization method the total counts from a measurement was given as the "slow count" in the file that is extracted from the XRF. Again, there were no uncertainties provided with the slow counts. Instead of a designated error, the square root of the value obtained from the normalization method was taken as the uncertainty for a given measurement for both ROI and TAR methods.

### **3.6.2 Uncertainty in Fe/Mo and Scatter Peak**

The uncertainty in the Fe/Mo method was given in the batch fit file as this normalization technique assumed the coherent peak was actually an elemental peak. The uncertainty in the Scatter Peak method was also produced in the batch fit file. PyMCA gave the error in the coherent peak in the same way as the elemental peaks.

## **3.7 Data comparison**

To compare the okra data, plots for each element were created with the ICP-MS concentrations on the x-axis and corresponding normalized counts on the y-axis. This was done for Ca, K, and P and using both energy beams. Linear trend lines were added and  $R^2$  values were examined. The  $R^2$  values for the two energy beams were first compared to observe which beam was more appropriate for these elements. The values were then compared within a beam for each normalization method and element to determine the best normalization technique for the lower Z elements.

The ICP-MS data for the goat horn only included Ca out of all three elements so it was the only element examined. Again, plots were created with the ICP-MS con-

centrations on the x-axis and normalized counts on the y-axis. Linear trend lines were added to compare  $R^2$  values to determine the optimal beam energy and normalization method.

Uncertainties of the normalized counts were determined in both okra and goat horn to help examine the reliability of the data and provide insight to possible conclusions. Concentrations provided directly by the XRF system (XOS concentrations) were also examined in comparison to the normalization methods.

## Chapter 4

### RESULTS

#### 4.1 Okra

Examples of the okra spectra produced by the relationship between counts output and the energy from the XRF system are shown in Figure 4.1 and Figure 4.2 using the 6.4 keV and 17.48 keV beams respectively for sample 50. Sample 50 of the okra is selected here as a typical representative sample. The red curves on the spectra are the PyMCA fittings to the energy range used in the configuration of the elements for both plots. The characteristic X-ray peaks of the three elements of interest are labeled on both graphs with Ca  $K_\alpha$  at 3.69 keV, P  $K_\alpha$  at 2.01 keV, and K  $K_\alpha$  at 3.31 keV.

In Figure 4.1, the spectrum of sample 50 of okra using the 6.4 keV beam for 180 seconds is displayed. The peak with the highest counts is K with its highest point at approximately 15,000, next is Ca at 6,500, and finally P at 200. The peak at 6.4 keV corresponds to the coherent peak with the Compton peak contributing to the coherent at a slightly lower energy. Above the coherent peak are small peaks representing Zn  $K_\alpha$  and Zn  $K_\beta$ . The peaks between 15.0 keV and 17.5 keV are the scatter peaks from the 17.48 keV beam passing through the iron target.

In Figure 4.2, the spectrum of sample 50 of okra using the 17.48 keV beam for 180 seconds is displayed. The elements have the same relationship as they did in Figure 4.1 though the counts for each peak decreased such that the peak count for K was 8,000, 3,000 for Ca, and 150 for P. The peaks between 5 keV and 10 keV are more substantial than in Figure 4.1. The largest peaks on the spectrum are the Compton

and coherent peak at 16.5 keV and 17.48 keV respectively. From these results, it is suggested that the low energy beam provides more fluorescent counts from Ca, P, and K.

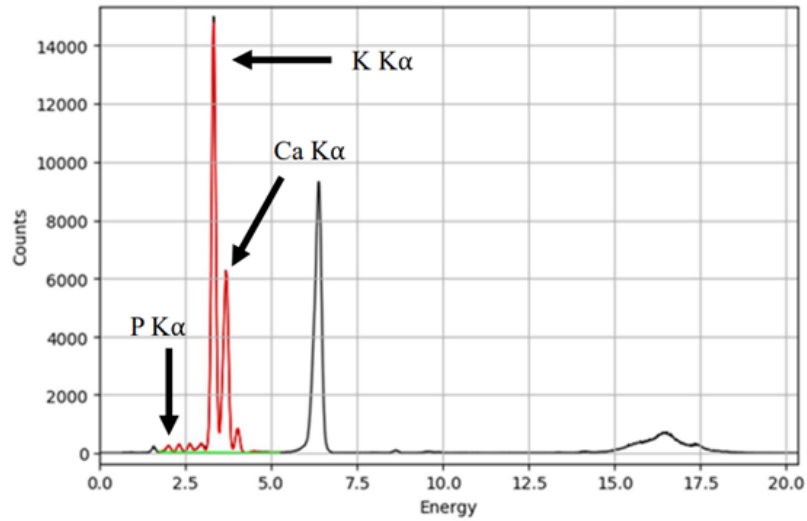


Figure 4.1: Spectrum of the energy (keV) and un-normalized counts for okra sample 50 using the 6.4 keV X-ray beam.

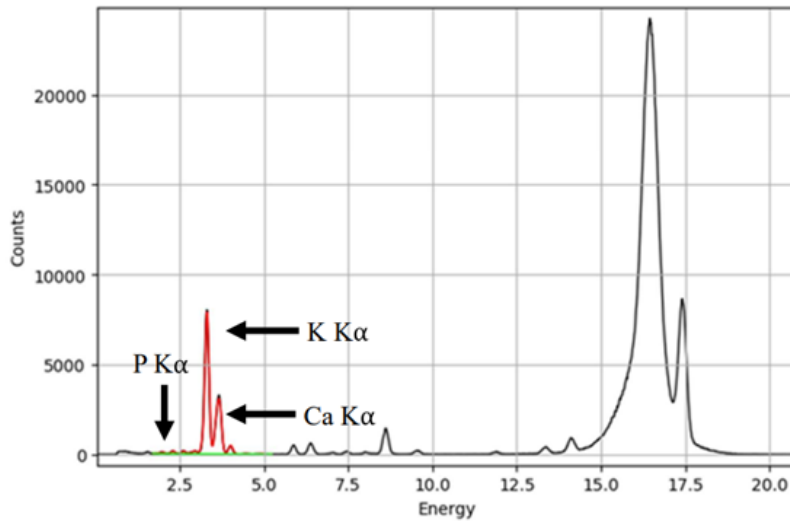


Figure 4.2: Spectrum of the energy (keV) and un-normalized counts for okra sample 50 using the 17.48 keV X-ray beam.

### 4.1.1 Calcium linear correlations

Calcium of the okra data using the low energy beam was examined by plotting the ICP-MS measurements on the x-axis in  $\mu\text{g/g}$  and the normalized calcium counts on the y-axis as seen in Figure 4.3. The four normalization methods were plotted with the best fit trend lines and  $R^2$  values added for each. The three methods of normalization that utilized the coherent peak have slopes greater than the method which used the total counts. The coherent normalizations are all in the same area of the plot while the TAR method is a tenth of the normalized counts. This result is expected since the TAR method normalizes against the largest value, the total counts. The best fitting trend line (by  $R^2$ ) to the data is the ROI method followed by Fe, Scatter peak, and finally TAR.

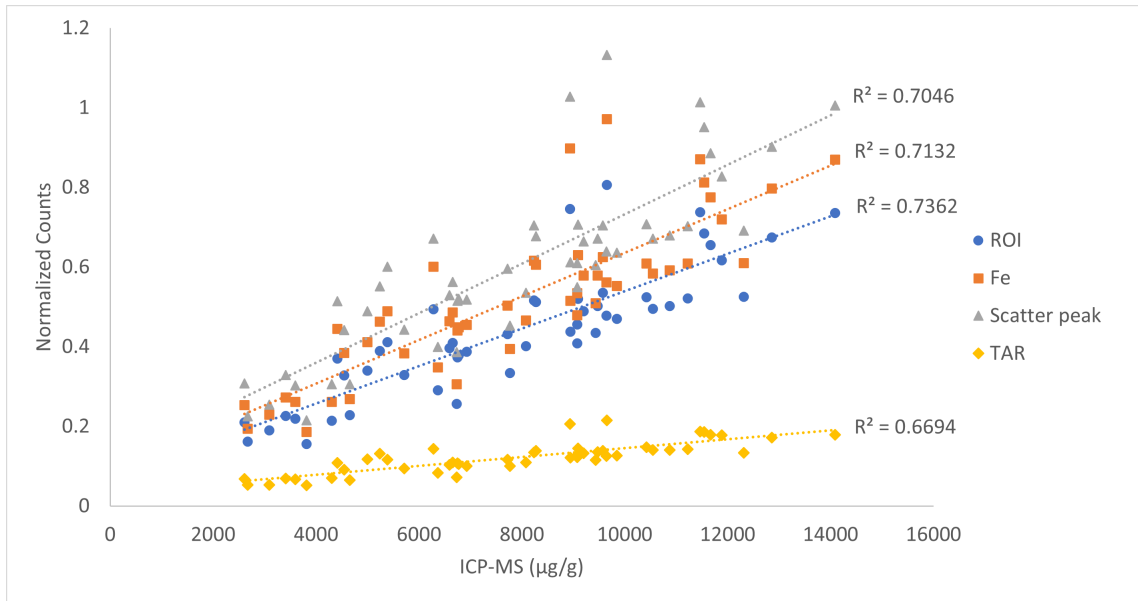


Figure 4.3: Normalization method comparison using the relationship between normalized counts and ICP-MS concentration of Ca in okra with the 6.4 keV X-ray beam.

Calcium of the okra data using the high energy beam was examined with the same method as seen in Figure 4.4. The slopes of the trend lines have the same overall

pattern as in Figure 4.3. However, the three sets of data using coherent normalization appear to have more scatter than TAR method which is confirmed by the  $R^2$  values. This is different than the result from Figure 4.3. The highest  $R^2$  corresponds to the TAR technique followed by ROI, Mo, and Scatter Peak. The ordering of  $R^2$  results was almost the same between the low energy and high energy beams. The TAR method which placed last in correlation for the low energy became the best correlation for the high energy beam.

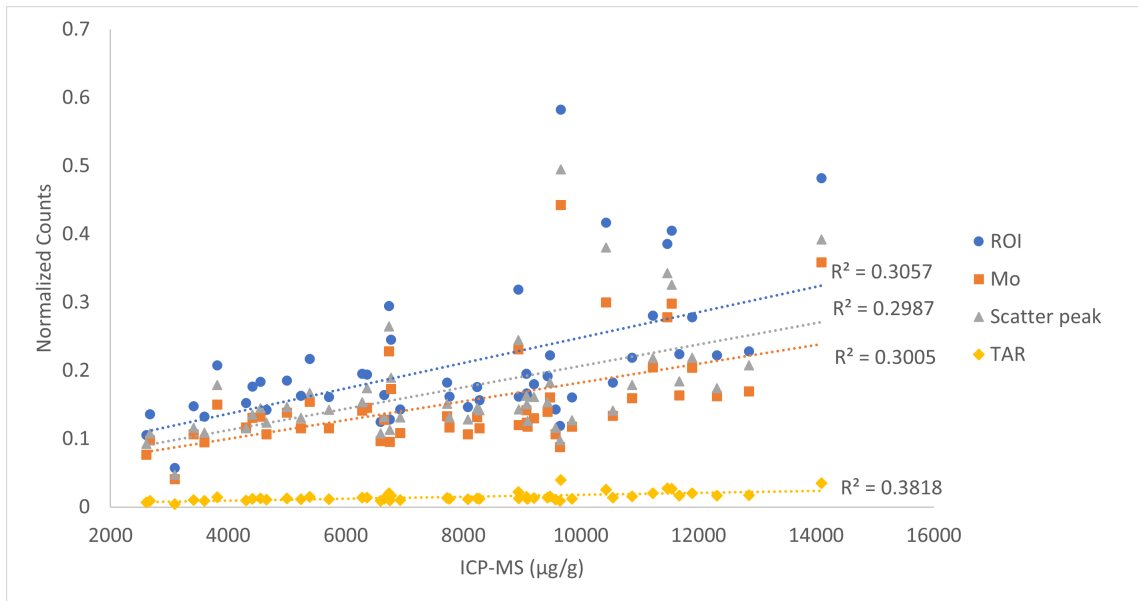


Figure 4.4: Normalization method comparison using the relationship between normalized counts and ICP-MS concentration of Ca in okra with the 17.48 keV X-ray beam.

#### 4.1.2 Phosphorus linear correlations

The relationship between the normalized P counts and ICP-MS for the okra using the low energy beam is depicted in Figure 4.5. The slopes of the trend lines have the same pattern as in Figure 4.3. The data for P has less scatter than Ca as shown in the  $R^2$  values. The highest  $R^2$  corresponds to the Fe normalization method followed by ROI, TAR, and Scatter peak.

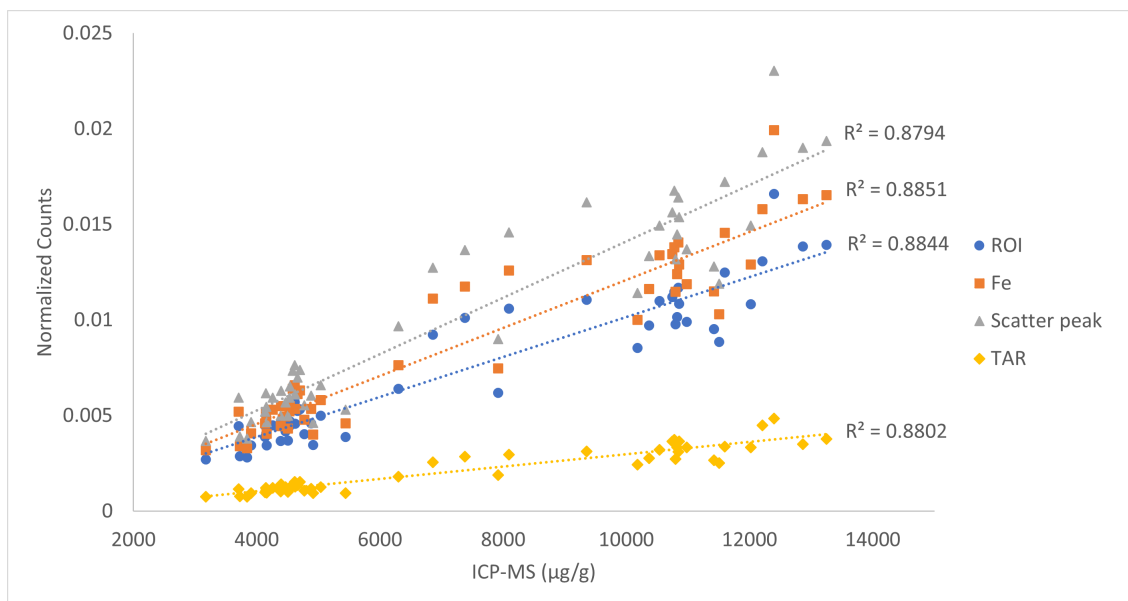


Figure 4.5: Normalization method comparison using the relationship between normalized counts and ICP-MS concentration of P in okra with the 6.4 keV X-ray beam.

The relationship between the normalized P counts and ICP-MS for the okra using the high energy beam is illustrated in Figure 4.6. TAR has a very shallow slope compared to the methods using the coherent scatter peak. The highest  $R^2$  corresponds to the ROI normalization method followed by TAR, Scatter peak, and Mo. The relative ordering of  $R^2$  results was almost the same between the low energy and high energy beams. The Fe/Mo method which had the best correlation to ICP-MS for the low energy became last in terms of correlation for the high energy beam. Though there appears to be a similar relationship as Ca in this regard, the order of the best normalization methods between the two elements is quite different.

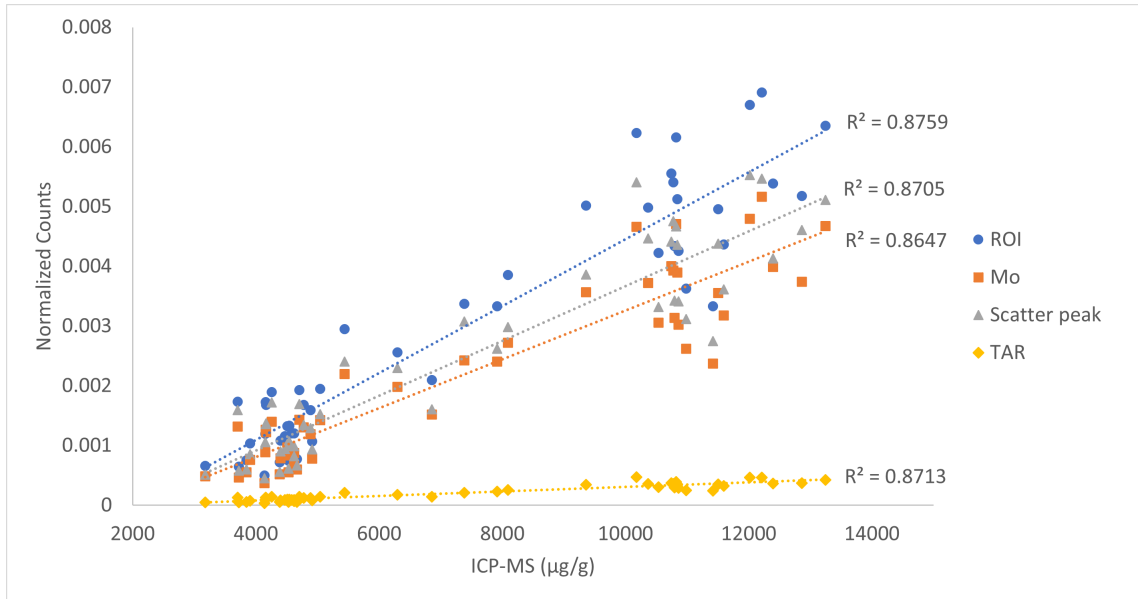


Figure 4.6: Normalization method comparison using the relationship between normalized counts and ICP-MS concentration of P in okra with the 17.48 keV X-ray beam.

### 4.1.3 Potassium linear correlations

Potassium was then examined using the same methods as the other elements. The relationship between the normalized K counts and ICP-MS for the okra using the low energy beam is shown in Figure 4.7. The data points for the coherent normalization method line up with each other well such that they have the same spread but vertically displaced from one another. The highest  $R^2$  corresponds to the ROI normalization method followed by Fe, Scatter peak, and TAR. These results are the same as those from Ca.

The relationship between the normalized K counts and ICP-MS for the okra using the high energy beam is shown in Figure 4.8. TAR has a very shallow slope compared to the methods using the coherent scatter peak again. There is an increase in scatter from the low energy beam as seen in the lowered  $R^2$  values. The highest  $R^2$  was for the TAR normalization method followed by Scatter peak, Mo, and ROI. These results

are quite different than those from Ca and P. The ranking of normalization methods by  $R^2$  reversed order between the low energy and high energy beams.

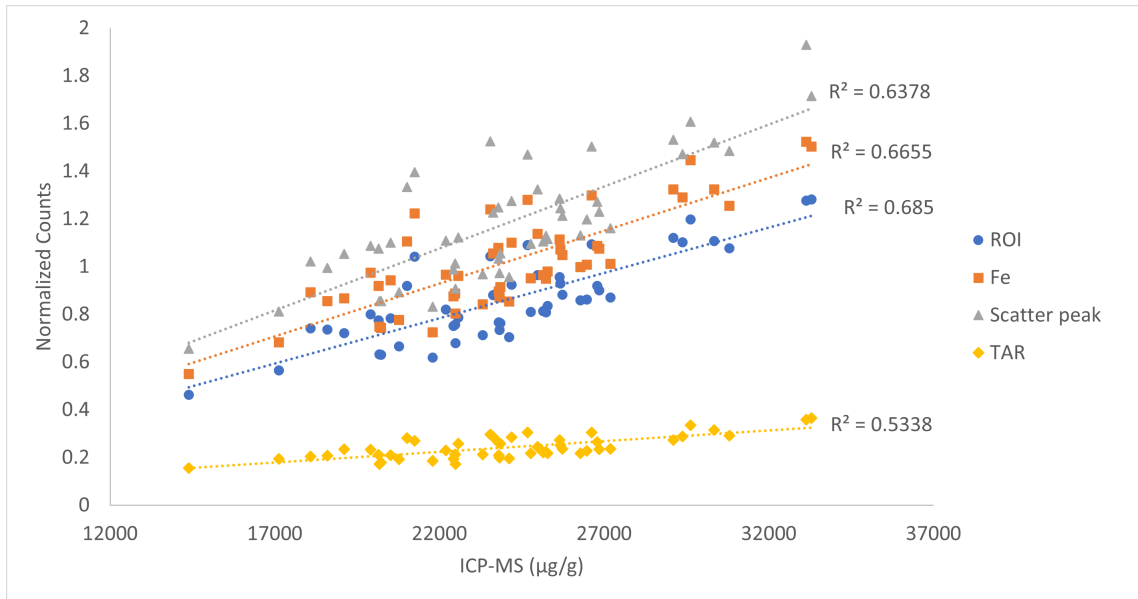


Figure 4.7: Normalization method comparison using the relationship between normalized counts and ICP-MS concentration of K in okra with the 6.4 keV X-ray beam.

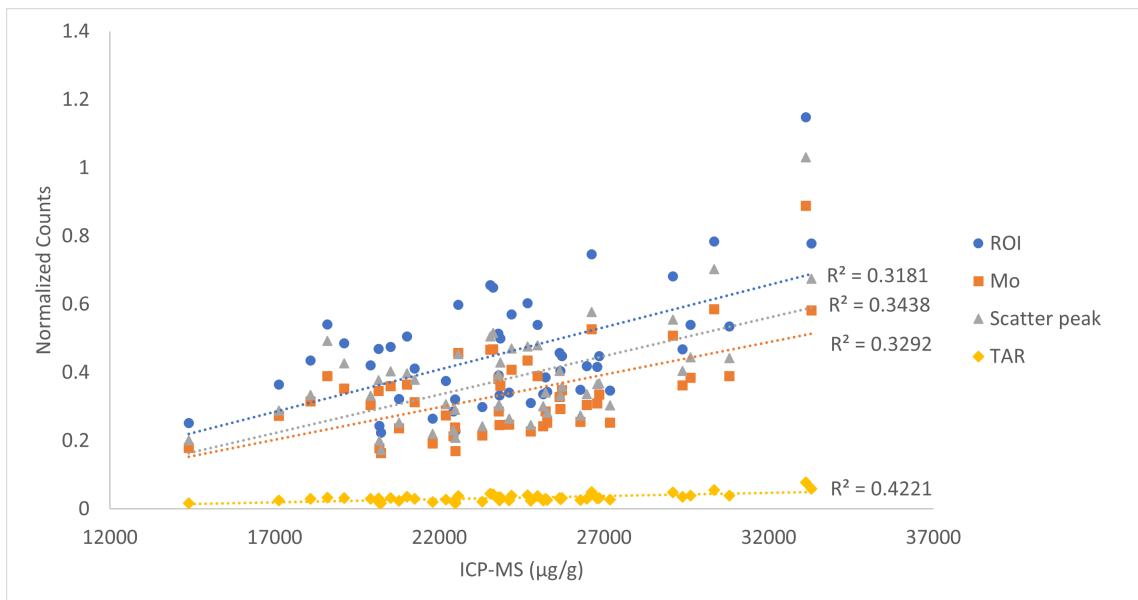


Figure 4.8: Normalization method comparison using the relationship between normalized counts and ICP-MS concentration of K in okra with the 17.48 keV X-ray beam.

The  $R^2$  values for linear correlations between normalized counts and ICP-MS results for each element and normalization method were compiled in Table 4.1 and Table 4.2 for the 6.4 keV and 17.48 keV beam respectively. The concentrations of the three elements of interest output by the XRF system directly (XOS concentrations), were also plotted against ICP-MS results and  $R^2$  recorded. The average  $R^2$  values for the low energy beam excluding XOS was 0.74. In Table 4.1, the normalization techniques with  $R^2$  values in order of highest to lowest were Fe for P, ROI for Ca, and ROI for K. The XOS concentrations had the lowest correlations of all techniques for the low energy X-ray beam. There were only 22 of 50 samples with XOS concentrations for P as the others reported no detection.

Element	ROI	Fe	Scatter Peak	TAR	XOS
Ca	0.7362	0.7132	0.7046	0.6694	0.5779
P	0.8844	0.8851	0.8794	0.8802	0.1936
K	0.6850	0.6655	0.6378	0.5338	0.4506

Table 4.1: Summary of  $R^2$  values for linear correlations of okra between normalized counts and ICP-MS results for each element and normalization method using the 6.4 keV X-ray beam.

In Table 4.2, the highest  $R^2$  values of the normalization techniques proposed in this study for each element corresponded to the following: ROI for P, TAR for K, and TAR for Ca. The average  $R^2$  values for the high energy beam excluding XOS was 0.52. The XOS concentrations gave the highest correlations to ICP-MS for all elements when using the high energy beam. There were only 32 of 50 samples with XOS concentrations for Ca as the others reported no detection and no concentrations were reported for P. Comparing the  $R^2$  values between the two energy beams and excluding the XOS concentrations, average values for the 6.4 keV beam were greater by a 1.4 fold-change than the 17.48 keV beam.

Uncertainties of the normalized counts were averaged across measurements and compiled for each normalization methods and element. The range of relative un-

Element	ROI	Mo	Scatter Peak	TAR	XOS
Ca	0.3057	0.3005	0.2987	0.3818	0.5923
P	0.8759	0.8647	0.8705	0.8713	-
K	0.3181	0.3292	0.3438	0.4221	0.4524

Table 4.2: Summary of  $R^2$  values for linear correlations of okra between normalized counts and ICP-MS results for each element and normalization method using the 17.48 keV X-ray beam.

certainties for the normalized counts and ICP-MS results were compiled in table Table 4.3. Uncertainty in the measurements could change the  $R^2$  values of the trend lines. Relative uncertainties in ICP-MS were between approximately 1-1.5% while in the Ca and K normalized counts using the low energy beam, uncertainties ranged from 0.4-0.9% and jumped to 7% for P. Using the high energy beam, the relative uncertainties were 0.5-0.9% for Ca and K and 22% for P.

Element	6.4 keV (%)	17.48 keV (%)	ICP-MS (%)
Ca	0.61-0.95	0.88-0.93	1.39
P	6.96-7.06	22.27	1.54
K	0.37-0.77	0.49-0.57	0.95

Table 4.3: Summary of relative uncertainties in normalized counts for okra using the 6.4 keV and 17.48 keV X-ray beam.

## 4.2 Caprine horn

Examples of the caprine horn spectra produced by the relationship between counts output and the energy from the XRF system are shown in Figure 4.9 and Figure 4.10 using the 6.4 keV and 17.48 keV beams respectively for sample 1. The spectra provided here represent typical results. The red curves on the spectra are the PyMCA fitting to the energy range used in the configuration of the elements for both plots. The characteristic X-ray peaks of the three elements of interest are labeled on both graphs with Ca  $K_\alpha$  at 3.69 keV, P  $K_\alpha$  at 2.01 keV, and K  $K_\alpha$  at 3.31 keV.

The spectrum using the 6.4 keV beam in Figure 4.9 shows the coherent scatter peak at 6.4 keV with the highest count peak and the Compton and coherent peaks resulting from the 17.48 keV beam passing through. Again, some element peaks are visible between the 6.4 keV and 17.48 keV peaks. Here, Ca, P, and K are a small fraction of the okra samples while the coherent peak in the goat horn is comparable to the K counts in okra. Calcium in the goat horn has the highest counts of the three elements examined.

The spectrum using the 17.48 keV beam in Figure 4.10 shows the coherent scatter peak at 17.48 keV and the Compton peak with the greatest counts just below. The peaks between 6.5 keV and 10.0 keV are more prominent than in the low energy spectrum. The elements of interest have roughly the same number of counts as the low energy beam spectrum but are dwarfed by the Compton peak.

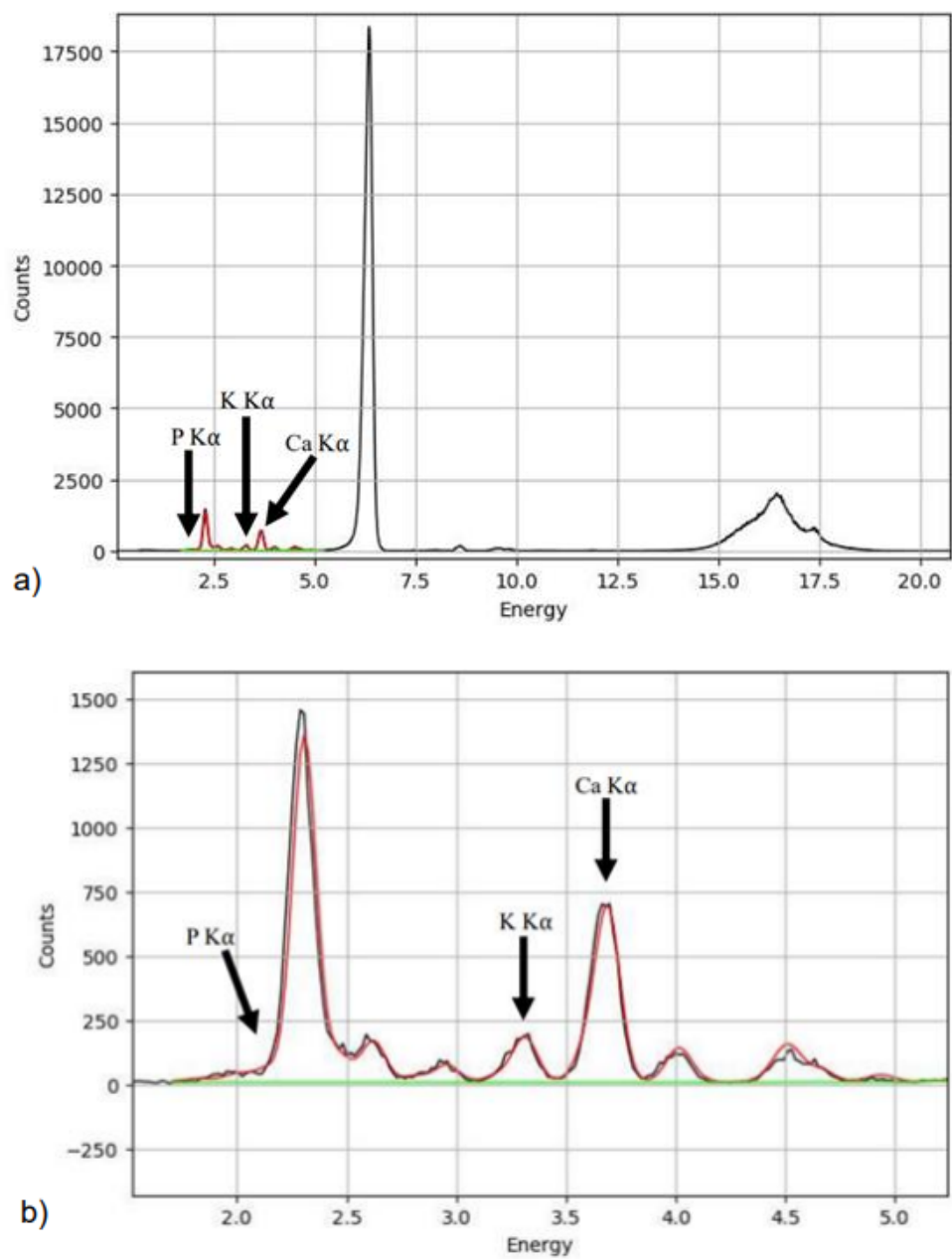


Figure 4.9: Spectrum of the un-normalized counts and energy (keV) for goat horn sample 1 using the 6.4 keV X-ray beam.

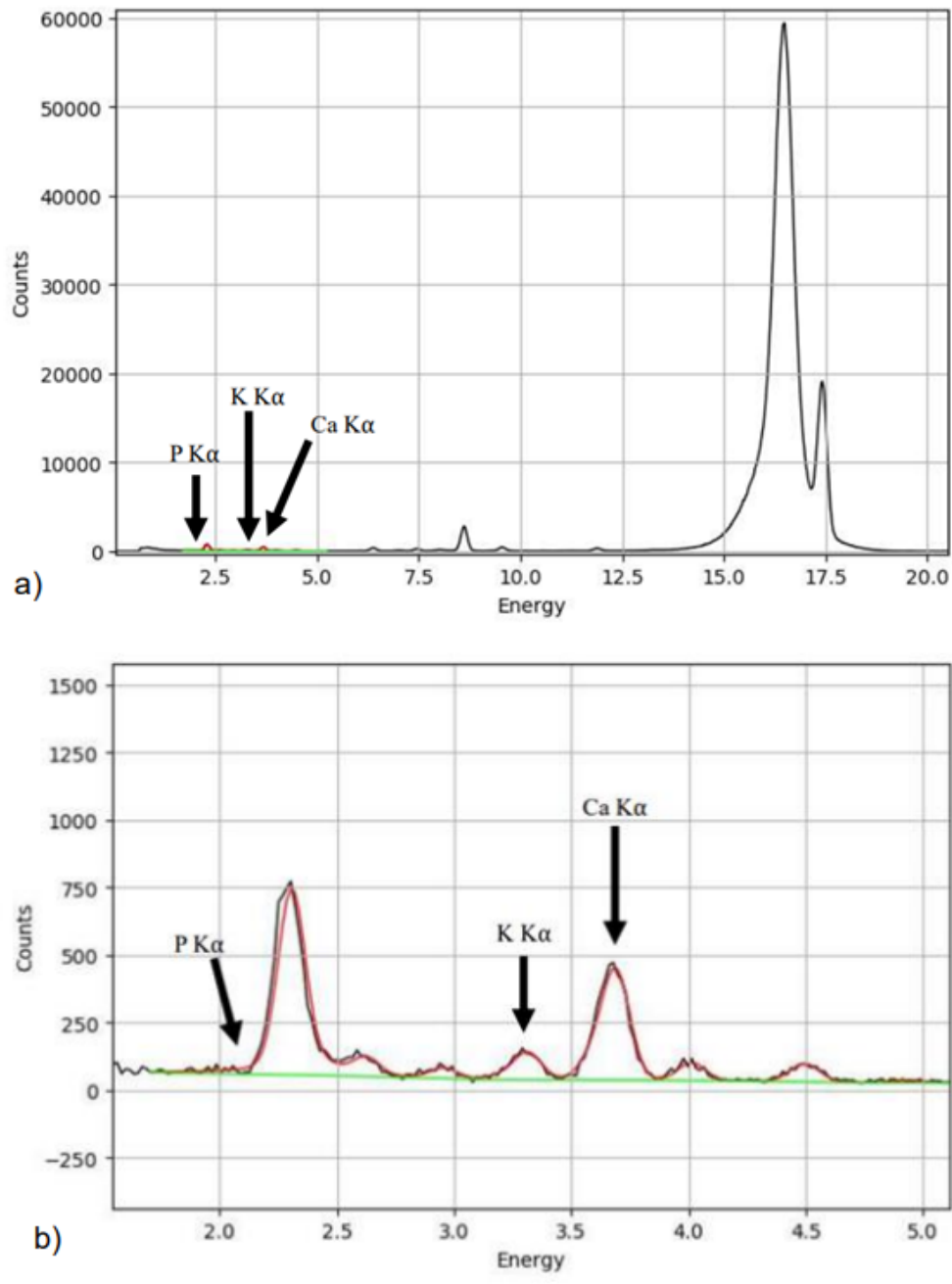


Figure 4.10: Spectrum of the un-normalized counts and energy (keV) for goat horn sample 1 using the 17.48 keV X-ray beam.

### 4.2.1 Low energy beam & high energy beam linear correlations

Only Ca was examined for the goat horn as it was the only element with ICP-MS results from the three elements of interest. Linear correlations between the normalized counts and ICP-MS results were plotted in Figure 4.11 while using the low energy beam and Figure 4.12 for high energy beam.

The Fe normalization methods using the 6.4 keV beam had the highest  $R^2$  value and TAR with the 17.48 keV beam had the lowest. All normalization techniques using the 6.4 keV beam are higher than their 17.48 keV counterparts. Unlike the okra results, there was a substantial difference between the  $R^2$  values of TAR and the methods using the coherent peak for the 6.4 keV X-ray beam. There was also a substantial difference between the  $R^2$  values of TAR compared to ROI, Mo, and Scatter peak while using the 17.48keV X-ray beam.

Again, the TAR method provided normalized counts that are lower than the methods using the coherent peak. There is a pronounced difference between the low energy and high energy plots when comparing the separation of the TAR and ROI trend lines. The maximum of the coherent peak is about 18,000 for the low energy spectra in Figure 4.9 a whereas the maximum value of the Compton peak in Figure 4.10 a is 60,000. The total counts while using the 17.48 keV beam are more than twice that of the 6.4 keV beam. This feature was not as noticeable in the okra data. All linear trend lines of the goat horn results have shallow slopes. Another key difference between the low and high energy beam linear correlations is the trend line directions. For the former, all slopes are positive like the okra, but for the latter, the coherent scatter normalization methods have negative slopes. This shows an inverse relationship between the high energy beam normalized counts and the ICP-MS concentrations. The relationship suggests that the coherent normalization is not ideal while using the high energy beam and examining low Z elements.

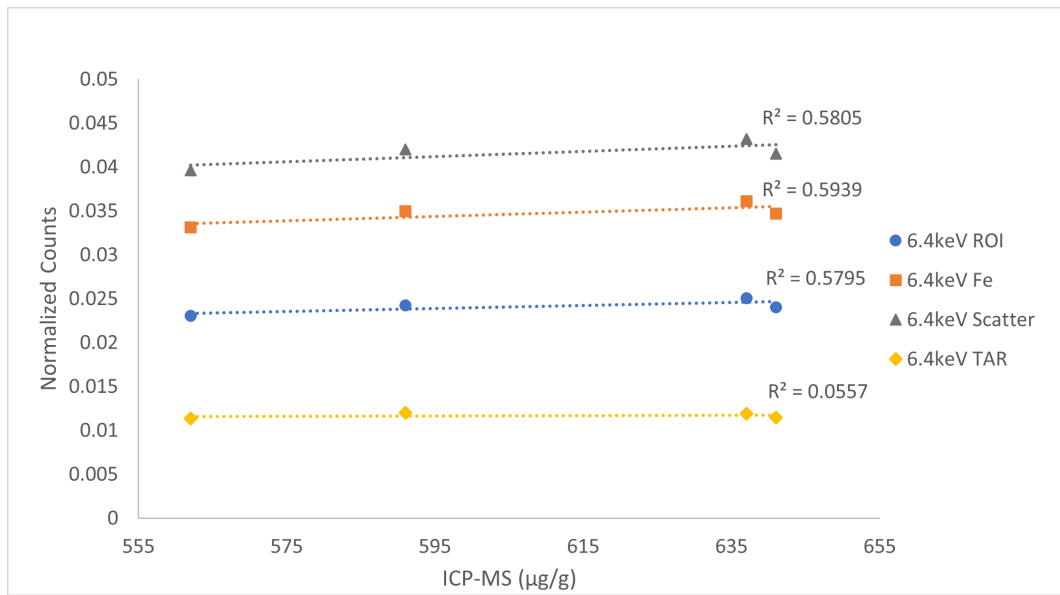


Figure 4.11: Normalization method comparison using the relationship between normalized counts and ICP-MS concentration of Ca in goat horn with the 6.4 keV X-ray beam.

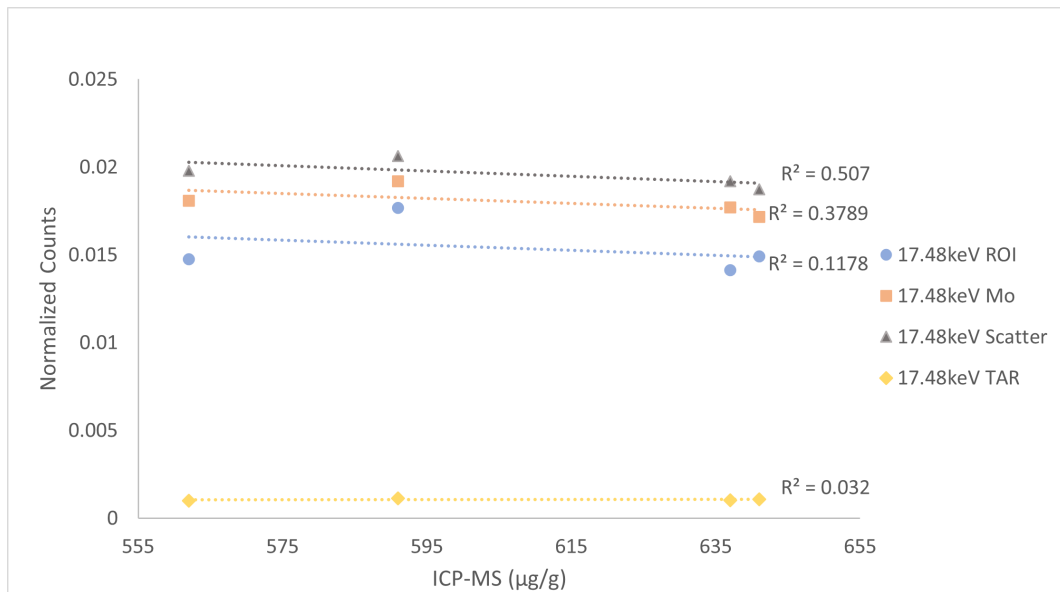


Figure 4.12: Normalization method comparison using the relationship between normalized counts and ICP-MS concentration of Ca in goat horn with the 17.48 keV X-ray beam.

The  $R^2$  values for linear correlations between normalized counts and ICP-MS results for Ca in goat horn with both 6.4 KeV and 17.48 keV beams are summarized in Table 4.4. XOS concentrations were again plotted against ICP-MS concentrations for Ca and  $R^2$  values recorded. The XOS did not detect any Ca while using the high energy beam. All  $R^2$  values were greater for the low energy beam. The average was 0.45 for the low energy beam and 0.26 for the high energy beam. The normalization techniques proposed in this study with  $R^2$  values in order of highest to lowest for the 6.4 keV beam were Fe, Scatter Peak, ROI, and TAR. The TAR method was smaller by a factor of 10 compared to the coherent normalizations. The XOS concentration had the lowest correlation to ICP-MS for the low energy beam, excluding the TAR method. Ranking the  $R^2$  values for the 17.48 keV beam are as follows: Scatter Peak, Mo, ROI, and TAR. TAR was smaller than the coherent peak methods by a factor of 10 once again.

Beam energy	ROI	Fe/Mo	Scatter Peak	TAR	XOS
6.4 keV	0.5795	0.5939	0.5805	0.0557	0.4769
17.48 keV	0.1178	0.3789	0.5070	0.0320	-

Table 4.4: Summary of  $R^2$  values for linear correlations of goat horn between normalized counts and ICP-MS results for Ca using each normalization method.

	Relative Uncertainty (%)
6.4 keV	1.96-2.06
17.48 keV	4.59-4.60
ICP-MS	2.5-5.6

Table 4.5: Summary of relative uncertainties in normalized counts for goat horn using the 6.4 keV and 17.48 keV X-ray beam.

Uncertainties of the normalized goat horn counts were averaged across all trials. The relative normalized count uncertainties in Table 4.5 show the range of values across the normalization methods where the ICP-MS uncertainty range is the range of the four samples. Uncertainty in the measurements could again change the  $R^2$

values of the trend lines. Relative uncertainties in ICP-MS were more varied than the okra, ranging between 2.5-5.6%. Using the low energy beam, uncertainties in normalized counts ranged from 1.96-2.06% and where they were 2.5-5.6% for for the high energy beam.

## Chapter 5

### DISCUSSION

The PyMCA spectra of okra and goat horn measured using the low energy beam show a large coherent peak at 6.4 keV with a Compton peak that is almost imperceptible just below at 6.24 keV. On the other hand, in the high energy beam graphs the Compton peak is 2.5 to 3 times larger than the coherent scatter peak. This follows the theory as the low energy X-rays have a relatively higher probability to scatter coherently than through Compton scatter. The probability of coherent scatter is increased for low energy X-rays that are less than 10 keV and for high atomic number elements. The probability is proportional to  $\frac{Z}{E^2}$  for coherent scatter [Gibbons and Khan, 2014].

#### 5.1 Low energy beam vs high energy beam

##### 5.1.1 Okra samples

The okra showed that  $R^2$  values were on average higher for the low energy beam indicating better correlation between the normalized counts and ICP-MS results. The average  $R^2$  for the low energy beam was 0.74 and for the high energy beam it was 0.52. P showed excellent correlation while using both beams which means P is an element that matched well with the ICP-MS data no matter which beam was used. The correlations for Ca and K were much higher for the low energy beam; the  $R^2$  values were twice the size as those from the high energy beam.

The okra data suggests that the low energy beam is better to use to analyse the low Z elements. This is evident through the high correlations for all three elements

examined in this study. Given the choice between the two excitation energies, the lower 6.4 keV beam should be used for low  $Z$  elements. The low energy beam has enough energy to excite elements up to chromium (Cr) but since the  $K_{\alpha}$  of Cr is close to that of Fe, the Cr element peak is in the tail end of the coherent peak. This affects the peak area that would be calculated by PyMCA and would provide inaccurate results. Therefore, the low energy beam is capable of determining the concentrations of elements below but not including Cr. From theory, the low energy beam was expected to perform well for low  $Z$  elements. Each electron shell in an atom has a minimum energy level that must be applied to remove an electron from that shell. The removal of an electron is most probable when exactly the amount of energy equal to the binding energy is transferred to the electron. When a higher energy beam hits the atoms in a sample, the probability that the electron is ejected decreases. The binding energy for the K electron shell of Ca is about 4.05 keV. The lower 6.4 keV X-ray beam is closer to this value than the higher 17.48 keV beam so therefore it is more effective at ejecting electrons from the low  $Z$  atoms.

The ICP-MS data for the three elements of interest along with Ca and K measured using the low energy X-ray beam had relative uncertainties of 1.5% or less. The relative uncertainty for P using the low energy beam was 7%, a clear contrast to the other results. Using the high energy beam, the uncertainties were less than 1% for Ca and K and 22% for P. The high uncertainties in P could be because it had a very low concentration in the samples and the XRF had difficulties detecting it. This again shows the low energy beam is the way to go but also that we may not be able to rely as confidently on the results from P.

### 5.1.2 Caprine horn samples

The goat horn data had  $R^2$  values that were on average higher for the low energy X-ray beam again, and showed that there is a better correlation between the normalized counts and ICP-MS results for the low energy beam. The average  $R^2$  for the low energy X-ray beam was 0.45 and for the high energy X-ray beam it was 0.26. The TAR method had poor correlation for both the low and high energy X-ray beams. The goat horn  $R^2$  values of Ca using the low energy beam were less than those from the okra but fairly close, and higher than the  $R^2$  values of Ca using the high energy beam.

The differences in  $R^2$  values between the the low energy and high energy beams shows an interesting relationship with normalization for the goat horns that was not apparent in the okra. In the okra, the  $R^2$  values of the normalization methods decreased to near the same value when using the high energy beam. In the goat horn, the  $R^2$  for the low energy beam and ROI normalization method was nearly 5 times larger than when using the high energy beam. The Fe/Mo  $R^2$  value for the low energy beam was 1.6 times larger than its high energy beam counterpart and the Scatter Peak had a 1.1-fold change between the low and high energy beams. All methods were the same as performed for the okra. One difference between the ROI and other methods for the goat horn is that the counts of the coherent peak are nearly the same between the low energy and high energy beam whereas there is a change of a few thousand counts between the beams for the Fe/Mo and Scatter Peak methods. The ROI counts of the goat horn are larger for the low energy beam than the high energy beam which is not the case for the other normalization methods or the okra. The reason for this is unknown but could explain the differences of  $R^2$  values between beam energies and normalization methods.

The relative uncertainties in the goat horn for the ICP-MS concentrations of Ca

ranged from 2.5%-5.6% whereas the XRF normalized counts had 2% for the low energy beam and approximately 4.6% for the high energy beam. Due to higher uncertainty in the goat horn measurements compared to the okra, the linear correlations could vary some and therefore are less definitive than the Ca results from okra.

## 5.2 Normalization method comparison

There is not a normalization method that is clearly the best for both low and high energy X-ray fluorescence excitation beams in the analysis of low atomic number elements. For these elements, the low energy beam has shown good correlations and was expected to provide better results. Therefore, more emphasis should be placed on low energy results in terms of normalization techniques as discussed below.

### 5.2.1 Okra samples using low energy beam

The  $R^2$  values for okra using the low energy beam were greatest for the ROI method of normalization in Ca and K and a close second to the Fe method for P.  $R^2$  values from each normalization for P were all close to each other in their respective beam energy. This suggests that P is an element that has excellent correlation with ICP-MS without preference of a normalization method.

The results from Ca and K in okra using the low energy beam indicate that the ROI method may provide the best results. For P, the best normalization was the Fe method but the other techniques provided similar  $R^2$  values and thus may not be the best evidence to conclude which is the optimal method. The preference for a method using coherent normalization is in agreement with a study that used TOPAS Monte Carlo code to investigate normalization techniques, which suggested the coherent normalization is a robust procedure and may be the optimal method [Sharma et al., 2022]. The study found that the TAR method was susceptible to error through

changes in the thickness of nail or sample. Although thickness of sample did not vary much in this study it could have contributed to small differences in results.

In the current study, the XOS methods did relatively poorly in the case of all three elements of interest when compared to the other normalization methods.

The primary study of the okra [Woldetsadik et al., 2021], provided concentrations of Ca and K using the values output from the XRF system itself without the need for normalization. The paper plotted XOS concentrations against the ICP-MS concentrations which gave  $R^2$  values of 0.66 and 0.27 for Ca and K respectively [Woldetsadik et al., 2021]. Both of these  $R^2$  values are lower than the ones determined here using the coherent peak normalization method and 6.4 keV X-ray beam. This suggests our normalization method using coherent scatter may be superior to the manufacturers' routine. P was not examined in the original okra study so could not be compared.

The  $R^2$  values of the XOS concentration relationship to ICP-MS from this study were lower for Ca and higher for K than those from the original paper [Woldetsadik et al., 2021]. The Ca XOS concentrations in the current study had less correlation to the ICP-MS results than the XOS concentrations from the okra study. However, the K XOS concentrations in the current study had higher correlation to the ICP-MS data than those from the primary okra paper.

The ROI normalization approach with the 6.4 keV X-ray beam may be the optimal method for the elements examined in this study though all normalization methods produced decent correlations for the low energy beam.

### **5.2.2 Okra samples using high energy beam**

The  $R^2$  values for the high energy beam were greatest for the TAR method in Ca and K and a close second to ROI for P. In this case, the TAR method had  $R^2$  values that were 1.2 times greater than the other techniques for both Ca and K. Again, P had a

similar result to the low energy beam where all  $R^2$  values were about the same so P may not indicate the optimal normalization method. Ca and K had similar  $R^2$  values but those for K were slightly higher which is unlike the low energy beam results.

The results from Ca and K in okra using the high energy beam suggest the TAR method may provide the best results out of the original four normalization methods. When considering the XOS concentrations, it has far higher  $R^2$  than the other methods; nearly twice the coherent normalizations for Ca and almost 1.5 times greater for K. XOS provides the best correlations to the ICP-MS concentrations of all the methods. These are conflicting results as the ROI method provided data with a higher correlation to the ICP-MS values for the low energy beam yet the TAR method gave closer trends to ICP-MS for the high energy beam out of the normalization methods.

The results using the normalization techniques and the high energy beam all did worse for Ca in the current study when compared with the primary okra study [Woldetsadik et al., 2021]. However, the normalization techniques in this study did better for K. This is the case for the XOS concentrations determined here as well.

### **5.2.3 Caprine horn samples using low energy beam**

The Fe normalization method had the best correlation to the ICP-MS concentrations for Ca while using the low energy X-ray beam with goat horns, but this may not be as accurate as the okra measurements. All normalization methods using the coherent peak had decent correlations while TAR had  $R^2$  values a tenth of the others. This indicates that TAR did poorly and the coherent peak normalization are better. The coherent peak normalization methods had  $R^2$  values that were similar to each other. The XOS concentrations had a correlation between the coherent peak normalization and the TAR method. Though the goat horn data suggests that the Fe method provides the best results, higher relative uncertainties compared to the okra data

mean that more weight and consideration should be given to the okra data. The relative uncertainties of the goat horn results were twice the size of the okra for the low energy beam. For this reason the goat horn data could be slightly different which would change the  $R^2$  values and suggest a different optimal normalization method.

The goat horn were initially created to be keratin reference materials and the Atlantic PATH studies using XRF examined zinc [Fleming et al., 2020] and arsenic [Fleming et al., 2021] concentrations in human nail clippings. The zinc study used the TAR normalization method and the XOS concentrations in comparison to ICP-MS concentrations through linear equations of best fit while using the high energy beam [Fleming et al., 2020]. They found plotting the TAR normalized counts against ICP-MS concentrations produced an  $R^2$  value of 0.46 [Fleming et al., 2020]. When plotting XOS concentrations versus ICP-MS concentrations the  $R^2$  was 0.37 [Fleming et al., 2020]. Both values show there is less correlation with the ICP-MS results for zinc in nail clippings than the coherent peak normalization methods for Ca in goat horn while using the low energy beam. The XOS concentrations found in the current study using the low energy X-ray beam did slightly better than the TAR normalization method in the Atlantic PATH zinc study. Plots were created in the Atlantic PATH arsenic study comparing TAR normalized arsenic counts to ICP-MS concentrations [Fleming et al., 2021]. The  $R^2$  values were 0.59 and 0.79 for using all 59 samples and 20 samples respectively [Fleming et al., 2021]. The 20 samples were isolated as they had normalized counts that were at least two times larger than the uncertainty for a given measurement [Fleming et al., 2021]. The trial with all 59 samples had nearly the same correlation to ICP-MS concentrations for arsenic using the high energy X-ray beam as the coherent normalization methods using the low energy beam for Ca, P, and K. On the other hand, the correlation of the 20 nail samples had better correlation for arsenic than all the normalization methods used

in the current study.

#### 5.2.4 Caprine horn samples using high energy beam

All coherent scatter normalization methods using the high energy beam for the goat horn gave negative slopes when plotted against ICP-MS concentrations. This indicates the method is not working either due to the use of the high energy beam or to the very limited variation in concentration between the 4 goat horn samples. This makes it more difficult to demonstrate the capabilities of the various measurement techniques. For example, concentrations of Ca varied from 2500  $\mu\text{g/g}$  to 14,000  $\mu\text{g/g}$  in the different okra samples, but only varied from 562  $\mu\text{g/g}$  to 641  $\mu\text{g/g}$  in the four different goat horn samples.

The Scatter Peak normalization method had the best correlation to the ICP-MS concentrations for Ca with the goat horn results while using the high energy X-ray beam. ROI did a fair bit worse than the Scatter Peak method as mentioned earlier. Closer examination of this would be needed to determine the cause as they both used the coherent peak area to normalize and initial inspection did not show any irregularities in the methods. No XOS concentrations were available for Ca because it reported as below detection limit. Again, the relative uncertainties for goat horn were higher than the okra but this time almost 5 times greater.

In the Atlantic PATH zinc study [Fleming et al., 2020], the  $R^2$  values show there is less correlation with the ICP-MS concentrations for zinc in nail clippings than the Scatter Peak normalization method for Ca in goat horn while using the high energy beam. The Mo normalization here for goat horn did a bit better than the XOS method in the zinc study of but not the TAR method [Fleming et al., 2020]. As for the Atlantic PATH arsenic study [Fleming et al., 2021], the correlations between the TAR normalized counts of arsenic in nail and the ICP-MS results were again better

than the methods used in the current study for goat horn.

The primary goat horn study [Tehrani et al., 2020], did not examine Ca using XRF but another study, Assessment of X-ray fluorescence capabilities for nail and hair matrices through zinc measurement in keratin reference materials, [Fleming et al., 2023], looked at zinc concentrations in the goat horn samples used in the current study. The 2023 paper plotted the normalized zinc counts using the TAR method against ICP-MS concentrations in  $\mu\text{g/g}$  [Fleming et al., 2023]. It was also repeated for the XOS concentrations against ICP-MS concentrations. Both plots showed correlations to the ICP-MS results that were much higher than those determined for Ca here. The  $R^2$  values were greater than 0.9 [Fleming et al., 2023]. Reasons that could explain the high  $R^2$  values in zinc is that it has a greater concentration in the samples and is a higher Z element so therefore it is easier to detect by the XRF. It could also be due to the little variation in concentration across the goat horn samples as previously mentioned.

## Chapter 6

### CONCLUSION

This study had the purpose of examining normalization techniques with low and high energy X-ray fluorescence excitation beams in the analysis of standard samples. Fifty okra samples and four goat horn samples were used as reference materials with known concentrations of low atomic number elements as determined by ICP-MS. Linear correlations between the XRF normalized counts and ICP-MS data showed the low energy X-ray beam provided better correlations than the high energy X-ray beam. Two of the three elements in okra showed that the ROI normalization technique using the 6.4 keV X-ray excitation could be the optimal method in the analysis of low atomic number elements. The last element, P, had excellent correlation in all cases but the Fe method using the low energy beam had the highest  $R^2$  value. This must be taken with a grain of salt because the uncertainty in the normalized counts were six times larger for P than the other elements. The best method for Ca in the goat horn was the Fe normalization using the low energy beam but all  $R^2$  values of the coherent normalization approaches were similar. The relative uncertainties in goat horn measurements were twice the size of the okra so the data could be slightly different changing the  $R^2$  values and suggesting another optimal normalization method.

This research is only valid for elements up to but not including chromium as the 6.4 keV beam does not have enough energy to create characteristic X-rays in higher Z elements. Most current studies are focused on higher Z elements while using XRF as they are heavier and easier to work with when using XRF. When the low Z elements are examined while using XRF, the system normally has a vacuum or partial vacuum

so there is no attenuation of photons coming into the detector and this allows for a stronger signal. This capability was not possible using our experimental apparatus.

Future work could include performing a similar experiment while using a system with a vacuum chamber. More research could be done by choosing elements at or above chromium and using the high energy beam with the various normalization techniques. This would provide more information as to whether the ROI or TAR normalization methods are better for the higher atomic number elements and thus confirm if the coherent peak is the optimal normalization technique in all situations.

## REFERENCES

- Aburto, N.J., Hanson, S., Gutierrez, H., Hooper, L., Elliott, P., Cappuccio, F.P., 2013. Effect of increased potassium intake on cardiovascular risk factors and disease: systematic review and meta-analyses. *BMJ* 346, f1378.
- Amanzadeh, J., Reilly, R.F., 2006. Hypophosphatemia: an evidence-based approach to its clinical consequences and management. *Nat Rev Nephrol* 2, 136–148.
- Bird, R.P., Eskin, N.A.M., 2021. Chapter Two - The emerging role of phosphorus in human health, in: Eskin, N.A.M. (Ed.), *Advances in Food and Nutrition Research, The Latest Research and Development of Minerals in Human Nutrition*. Academic Press, pp. 27–88.
- Bose, S., French, S., Evans, F.J., Joubert, F., Balaban, R.S., 2003. Metabolic Network Control of Oxidative Phosphorylation: MULTIPLE ROLES OF INORGANIC PHOSPHATE\*. *Journal of Biological Chemistry* 278, 39155–39165.
- Cabral, B.M.I., Edding, S.N., Portocarrero, J.P., Lerma, E.V., 2020. Rhabdomyolysis. *Disease-a-Month, Rhabdomyolysis* 66, 101015.
- Calvo, M.S., Lamberg-Allardt, C.J., 2015. Phosphorus. *Advances in Nutrition* 6, 860–862.
- Calvo, M.S., Tucker, K.L., 2013. Is phosphorus intake that exceeds dietary requirements a risk factor in bone health? *Annals of the New York Academy of Sciences* 1301, 29–35.
- Calvo, M.S., Uribarri, J., 2013. Contributions to Total Phosphorus Intake: All Sources Considered. *Seminars in Dialysis* 26, 54–61.
- CDC, 2022. About Stroke. Centers for Disease Control and Prevention.
- CDC, 2021. High Blood Pressure Symptoms, Causes, and Problems. Centers for Disease Control and Prevention.
- Chang, A.R., Anderson, C., 2017. Dietary Phosphorus Intake and the Kidney. *Annu Rev Nutr* 37, 321–346.
- Chen, Z.W., Gibson, W.M., Huang, H., 2008. High Definition X-Ray Fluorescence: Principles and Techniques. *X-Ray Optics and Instrumentation* 2008, 10.

- Cormick, G., Ciapponi, A., Cafferata, M.L., Belizán, J.M., 2015. Calcium supplementation for prevention of primary hypertension. *Cochrane Database Syst Rev* 2015, CD010037.
- Dutton, J.J., 2010. Computed Tomography, in: Dutton, J.J. (Ed.), *Radiology of the Orbit and Visual Pathways*. W.B. Saunders, London, pp. 1–8.
- Ekmekcioglu, C., Elmadfa, I., Meyer, A.L., Moeslinger, T., 2016. The role of dietary potassium in hypertension and diabetes. *J Physiol Biochem* 72, 93–106.
- Elbanna, K.Y., Bahar, M., Achille, M., Patrik, R., Luís, S.G., 2020. Dual-energy CT in diffuse liver disease: is there a role? *Abdominal Radiology* 45, 3413–3424.
- Eremin, Y.A., 2005. Scattering Theory, in: Guenther, R.D. (Ed.), *Encyclopedia of Modern Optics*. Elsevier, Oxford, pp. 326–330. Evans, 2020. X-Ray Fluorescence Methods for Zinc Assessment in Nail Clippings. Mount Allison University.
- Fardellone, P., Séjourné, A., Blain, H., Cortet, B., Thomas, T., 2017. Osteoporosis: Is milk a kindness or a curse? *Joint Bone Spine* 84, 275–281.
- Fleming, D.E.B., 2022. The measurement of trace elements in human nails and nail clippings using portable X-ray fluorescence: A review. *X-Ray Spectrometry* 51, 328–337.
- Fleming, D.E.B., Crook, S.L., Evans, C.T., Nader, M.N., Atia, M., Hicks, J.M.T., Sweeney, E., McFarlane, C.R., Kim, J.S., Keltie, E., Adisesh, A., 2021. Assessing arsenic in human toenail clippings using portable X-ray fluorescence. *Applied Radiation and Isotopes* 167, 109491.
- Fleming, D.E.B., Crook, S.L., Evans, C.T., Nader, M.N., Atia, M., Hicks, J.M.T., Sweeney, E., McFarlane, C.R., Kim, J.S., Keltie, E., Adisesh, A., 2020. Portable X-ray fluorescence of zinc applied to human toenail clippings. *Journal of Trace Elements in Medicine and Biology* 62, 126603.
- Fleming, D.E.B., Kaiser, M.G., Rankin, B.D., Schenkels, K.M.M., 2023. Assessment of X-ray fluorescence capabilities for nail and hair matrices through zinc measurement in keratin reference materials. *Journal of Trace Elements in Medicine and Biology* 77, 127136.
- Gemedé, H.F., Ratta, N., Haki, G.D., Beyene, A.Z.W.F., 2014. Nutritional Quality and Health Benefits of Okra (*Abelmoschus Esculentus*): A Review. *Global Journal of Medical Research: K Interdisciplinary* 14.

- Gibbons, J.P., Khan, F.M., 2014. Khan's The Physics of Radiation Therapy. Lippincott Williams & Wilkins, Philadelphia.
- Guo, Y., Yan, S., Zhang, S., Zhang, X., Chen, Q., Liu, K., Liebeskind, D.S., Lou, M., 2015. Lower serum calcium level is associated with hemorrhagic transformation after thrombolysis. *Stroke* 46, 1359–1361.
- Gutiérrez, O.M., 2013. The Connection between Dietary Phosphorus, Cardiovascular Disease, and Mortality: Where We Stand and What We Need to Know. *Advances in Nutrition* 4, 723–729.
- He, F.J., MacGregor, G.A., 2008. Beneficial effects of potassium on human health. *Physiologia Plantarum* 133, 725–735.
- Hessenbruch, A., 2002. A brief history of x-rays. *Endeavour* 26, 137–141.
- J. E. Fernández, 1995. Polarization effects and gamma transport. *Applied Radiation and Isotopes* 46, 383–400.
- Jackson, W.F., 2017. Chapter Three - Potassium Channels in Regulation of Vascular Smooth Muscle Contraction and Growth, in: Khalil, R.A. (Ed.), *Advances in Pharmacology, Vascular Pharmacology*. Academic Press, pp. 89–144.
- Johnson, W., Onuma, O., Owolabi, M., Sachdev, S., 2016. Stroke: a global response is needed. *Bull World Health Organ* 94, 634-634A.
- Judd, S.E., Tangpricha, V., 2009. Vitamin D Deficiency and Risk for Cardiovascular Disease. *Am J Med Sci* 338, 40–44.
- Kendrick, J., Kestenbaum, B., Chonchol, M., 2011. Phosphate and Cardiovascular Disease. *Advances in Chronic Kidney Disease, What's New in Phosphate Homeostasis?* 18, 113–119.
- Kim, M.-H., Bu, S.Y., Choi, M.-K., 2012. Daily calcium intake and its relation to blood pressure, blood lipids, and oxidative stress biomarkers in hypertensive and normotensive subjects. *Nutr Res Pract* 6, 421–428.
- Kim, M.J., Valerio, C., Knobloch, G.K., 2023. Potassium Disorders: Hypokalemia and Hyperkalemia. *American Family Physician* 107, 59.
- Kowey, P.R., 2002. The Role of Potassium, in: Lobo, R.A., Crosignani, P.G., Paoletti, R., Bruschi, F. (Eds.), *Women's Health and Menopause: New Strategies —*

- Improved Quality of Life, Medical Science Symposia Series. Springer US, Boston, MA, pp. 151–157.
- Kvick, Å., 1999. Materials Science Applications of X-ray Diffraction, in: Lindon, J.C. (Ed.), *Encyclopedia of Spectroscopy and Spectrometry*. Elsevier, Oxford, pp. 1248–1257.
- Lanham-New, S.A., Lambert, H., Frassetto, L., 2012. Potassium. *Advances in Nutrition* 3, 820–821.
- Mahamid, J., Sharir, A., Gur, D., Zelzer, E., Addadi, L., Weiner, S., 2011. Bone mineralization proceeds through intracellular calcium phosphate loaded vesicles: A cryo-electron microscopy study. *Journal of Structural Biology* 174, 527–535.
- Margaritondo, G., 2005. Valence Photoemission, in: Bassani, F., Liedl, G.L., Wyder, P. (Eds.), *Encyclopedia of Condensed Matter Physics*. Elsevier, Oxford, pp. 279–286.
- Margui, E., Van Grieken, R., 2013. *X-Ray Fluorescence Spectrometry and Related Techniques: An Introduction*. Momentum Press. Markus, H., 2008. Stroke: causes and clinical features. *Medicine, Neurology Part 2 of 3* 36, 586–591.
- McCarron, D.A., Morris, C.D., Cole, C., 1982. Dietary Calcium in Human Hypertension. *Science* 217, 267–269.
- Michigami, T., Kawai, M., Yamazaki, M., Ozono, K., 2018. Phosphate as a Signaling Molecule and Its Sensing Mechanism. *Physiological Reviews* 98, 2317–2348.
- Michigami, T., Ozono, K., 2019. Roles of Phosphate in Skeleton. *Frontiers in Endocrinology* 10.
- Miller, G.D., Jarvis, J.K., McBean, L.D., 2001. The Importance of Meeting Calcium Needs with Foods. *Journal of the American College of Nutrition* 20, 168S-185S.
- National Institute on Aging, n.d. Osteoporosis. National Institute of Health.
- Office of Dietary Supplements, 2021. Phosphorus. National Institute of Health.
- Palta, S., Saroa, R., Palta, A., 2014. Overview of the coagulation system. *Indian J Anaesth* 58, 515
- Parham, W.A., Mehdirad, A.A., Biermann, K.M., Fredman, C.S., 2006. Hyperkalemia Revisited. *Tex Heart Inst J* 33, 40–47.

- Pohl, H.R., Wheeler, J.S., Murray, H.E., 2013. Sodium and Potassium in Health and Disease, in: Sigel, A., Sigel, H., Sigel, R.K.O. (Eds.), *Interrelations between Essential Metal Ions and Human Diseases, Metal Ions in Life Sciences*. Springer Netherlands, Dordrecht, pp. 29–47.
- Pu, F., Chen, N., Xue, S., 2016. Calcium intake, calcium homeostasis and health. *Food Science and Human Wellness* 5, 8–16.
- Qadeer, H.A., Bashir, K., 2022. Physiology, Phosphate, in: *StatPearls*. StatPearls Publishing, Treasure Island (FL).
- Reid, I.R., Bolland, M.J., Avenell, A., Grey, A., 2011. Cardiovascular effects of calcium supplementation. *Osteoporos Int* 22, 1649–1658.
- Sharma, U., Van Delinder, K., Gräfe, J.L., Fleming, D.E.B., 2022. Investigating methods of normalization for X-ray fluorescence measurements of zinc in nail clippings using the TOPAS Monte Carlo code. *Applied Radiation and Isotopes* 182, 110151.
- Smith, N.V., 2000. Science with soft X-rays. *Physics Today* 54.
- Stacy, J.G., Vestrand, W.T., 2003. Gamma-Ray Astronomy, in: Meyers, R.A. (Ed.), *Encyclopedia of Physical Science and Technology (Third Edition)*. Academic Press, New York, pp. 397–432.
- Sunycz, J.A., 2008. The use of calcium and vitamin D in the management of osteoporosis. *Ther Clin Risk Manag* 4, 827–836.
- Szent-Györgyi, A.G., 1975. Calcium regulation of muscle contraction. *Biophysical Journal, Thermodynamics of living systems: A special issue dedicated to Aharon Katchalsky* 15, 707–723.
- Takeda, E., Ikeda, S., Nakahashi, O., 2012. [Lack of phosphorus intake and nutrition]. *Clin Calcium* 22, 1487–1491.
- Takeda, E., Taketani, Y., Sawada, N., Sato, T., Yamamoto, H., 2004. The regulation and function of phosphate in the human body. *BioFactors* 21, 345–355.
- Tehrani, M.W., Yang, K.X., Parsons, P.J., 2020. Development and characterization of reference materials for trace element analysis of keratinized matrices. *Anal Bioanal Chem* 412, 1847–1861.

- Theobald, H.E., 2005. Dietary calcium and health. *Nutrition Bulletin* 30, 237–277.
- Uribarri, J., Calvo, M.S., 2014. Dietary phosphorus intake and health. *The American Journal of Clinical Nutrition* 99, 247–248.
- Vorland, C.J., Stremke, E.R., Moorthi, R.N., Hill Gallant, K.M., 2017. Effects of Excessive Dietary Phosphorus Intake on Bone Health. *Curr Osteoporos Rep* 15, 473–482.
- Weaver, C.M., Gordon, C.M., Janz, K.F., Kalkwarf, H.J., Lappe, J.M., Lewis, R., O’Karma, M., Wallace, T.C., Zemel, B.S., 2016. The National Osteoporosis Foundation’s position statement on peak bone mass development and lifestyle factors: a systematic review and implementation recommendations. *Osteoporos Int* 27, 1281–1386.
- Weindorf, D.C., Chakraborty, S., 2020. Portable X-ray fluorescence spectrometry analysis of soils. *Soil Science Society of America Journal* 84, 1384–1392.
- Whitaker, M., Larman, M.G., 2001. Calcium and mitosis. *Seminars in Cell & Developmental Biology* 12, 53–58.
- Woldetsadik, D., Llorent-Martínez, E.J., Gebrezgabher, S., Njenga, M., Mendum, R., Castillo-López, R., Fernández-de Córdoba, M.L., Hailu, H., Evans, C.T., Madani, N., Mafika, T.P., Fleming, D.E.B., 2021. Okra (*Abelmoschus esculentus*) in a refugee context in East Africa: Kitchen gardening helps with mineral provision. *SN Appl. Sci.* 4, 32.
- X-ray Optical Systems, 2008. *Doubly Curved Crystals For Monochromatic Micro X-ray Fluorescence and X-ray Diffraction*.
- Yamashita, S., Fujiwara, M., Kato, Y., Yamaguchi, T., Wakita, H., Adachi, H., 1998. X-Ray Absorption Near Edge Structure Study and DV-X $\alpha$  Calculations on Some Square-planar Copper(II) Complexes with Macrocyclic Ligands, in: Löwdin, P.-O., Sabin, J.R., Zerner, M.C., Brändas, E., Kövér, L., Kawai, J., Adachi, H. (Eds.), *Advances in Quantum Chemistry*. Academic Press, pp. 357–371.